Journal of Asian Earth Sciences 41 (2011) 383–400

Contents lists available at ScienceDirect

Journal of Asian Earth Sciences

journal homepage: www.elsevier.com/locate/jseaes

Pre-earthquake signals: Underlying physical processes

Friedemann Freund *

NASA Ames Research Center, MS 242-4, Moffett Field, CA 94035-1000, United States
Department of Physics, San Jose State University, San Jose, CA 95192-0196, United States
Carl Sagan Center (CSC), SETI Institute, 515 N Whisman Rd, Mountain View, CA 94043, United States

ARTICLE INFO

Article history:
Available online 9 April 2010

Keywords:
Earthquake
Pre-earthquake signals
Peroxy
Positive holes
EM emissions
Air ionization
Thermal infrared anomalies

ABSTRACT

Prior to large earthquakes the Earth sends out transient signals, sometimes strong, more often subtle and fleeting. These signals may consist of local magnetic field variations, electromagnetic emissions over a wide range of frequencies, a variety of atmospheric and ionospheric phenomena. Great uncertainty exists as to the nature of the processes that could produce such signals, both inside the Earth's crust and at the surface. The absence of a comprehensive physical mechanism has led to a patchwork of explanations, which are not internally consistent. The recognition that most crustal rocks contain dormant electronic charge carriers in the form of peroxy defects, $O_3Si/^{OO}\backslash SiO_3$, holds the key to a deeper understanding of these pre-earthquake signals from a solid state physics perspective. When rocks are stressed, peroxy links break, releasing electronic charge carriers, $h^{\cdot}$, known as positive holes. The positive holes are highly mobile and can flow out of the stressed subvolume. The situation is similar to that in a battery. The $h^{\cdot}$ outflow is possible when the battery circuit closes. The $h^{\cdot}$ outflow constitutes an electric current, which generates magnetic field variations and low frequency EM emissions. When the positive holes arrive at the Earth's surface, they lead to ionization of air at the ground–air interface. Under certain conditions corona discharges occur, which cause RF emission. The upward expansion of ionized air may be the reason for perturbations in the ionosphere. Recombination of $h^{\cdot}$ charge carriers at the surface leads to a spectroscopically distinct, non-thermal IR emission.

1. Introduction

1.1. Diversity of non-seismic pre-earthquake signals

For over a hundred years seismology has provided precious insight into the hidden structures of the Earth, into the distribution and orientation of tectonic faults in the Earth's crust and into the mechanics of earthquakes. However, earthquake forecasting is not an area where seismology excels. The reason is that the seismology is basically a historical science that bases its approach to earthquake "prediction" on the analysis of data from past events, large and small, and on the attempt to find patterns in their spatial and temporal distribution along given faults. This information is used to derive probability models for future events. No statistical approach can ever pinpoint the time, location and magnitude of a future event (Console et al., 2002; Grunewald and Stein, 2006; Stewart, 2000). This has led to statements such as "earthquakes cannot be predicted" (Geller et al., 1997; Mulargia and Geller, 2003).

The build-up of tectonic stress causes earthquakes. Broadly speaking, seismology is focusing on the mechanics of rupture, studying the spatial and temporal distribution of earthquakes, small and large, often combined with geodesic measurements to record deformation at the Earth surface or strain changes in the shallow crust. For rocks to fail under the onslaught of stress and cause a seismic signal, even a small one, the local stress levels must already have reached relatively high values, leading up to the critical point. What happens before this point remains largely a mystery.

The literature is replete with reports that, prior to major seismic events, the Earth sends out non-seismic, non-geodesic signals, sometimes strong, more often subtle and fleeting. They fall into a wide range of categories: magnetic field variations, seismo-electric signals (SES), electromagnetic (EM) emissions from VIS through IR and RF to ULF/ELF, various atmospheric and ionospheric phenomena, anomalous animal behavior, and others. If we want to develop the capability to forecast earthquakes beyond what is presently possible, we need to understand the causes of these very different phenomena and – importantly – how they may be linked to each other or correlated.

There have been many attempts in the past to explain how the different types of pre-earthquake signals might be generated (for a

* Address: NASA Ames Research Center, MS 242-4, Moffett Field, CA 94035-1000, United States. Tel.: +1 650 604 5183; fax: +1 650 604 4680.
E-mail address: friedemann.t.freund@nasa.gov

1367-9120/$ - see front matter © 2010 Elsevier Ltd. All rights reserved.
doi:10.1016/j.jseaes.2010.03.009

recent review see Uyeda et al. (2009b)). To account for EM signals, in particular for low frequency emissions, and seismo-electric signals, a number of well-known physical processes has been invoked such as microfracturing (Balbachan and Tomashevskaya, 1987; Brady and Rowell, 1986; Brady, 1992; Enomoto and Hashimoto, 1990; Hayakawa and Molchanov, 1998; Lebedev et al., 2003; Tzanis et al., 2000; Warwick et al., 1982), the piezoelectric effect (Bishop, 1981; Finkelstein et al., 1973; Huang, 2002; Ogawa and Utada, 2000a; Tuck et al., 1977), the electret effect (Balbachan and Parkhomenko, 1983), the piezomagnetic effect (Sasai, 1979, 1991, 2001; Stacey and Johnston, 1972; Zlotnicki and Cornet, 1986), the electrokinetic effect (Bernabé, 1998; Merzer and Klemperer, 1997; Morrison et al., 1989; Takahashi et al., 2007; Teisseyre, 1983), exo-electron emission (Brady and Rowell, 1986; Enomoto et al., 1993), and transient defects in condensed matter (Uyeda et al., 2009a; Varotsos et al., 1986; Varotsos and Alexopoulos, 1987; Varotsos, 2005).

To account for pre-earthquake "thermal infrared" (TIR) anomalies, CO_2 emanation leading to a local greenhouse effect or latent heat due to condensation of water on air ions formed as the result of radon emanation have been considered (Cervone et al., 2006; Ouzounov et al., 2006; Ouzounov et al., 2007; Pulinets and Dunajeck, 2006; Tronin, 1999).

To account for perturbations in the ionosphere, changes the conductivity of the near-ground air have been invoked, primarily due to radon emanation (Pulinets, 2007, 2009; Pulinets et al., 1997; Tronin, 1999). To account for unusual animal behavior low-frequency vibrations, high electric or magnetic fields have been proposed (Ikeya et al., 1996; Kirschvink, 2000; Logan, 1977; Milne and Lee, 1939; Schall, 1988; Turcotte, 1991).

1.2. Critique of conventional explanations of non-seismic pre-earthquake signals

This brief and necessarily incomplete review of published attempts to find explanations for the various pre-earthquake signals exposes two weaknesses: (i) to rationalize the range of reported precursors very different physical processes are invoked, which often have no clear communality or causal linkage and (ii) many of the proposed processes do not stand up to scrutiny as to their effectiveness in producing the signals which they are supposed to explain.

The idea of microfracturing has been inspired by laboratory experiments in the course of which unconstrained rock cylinders were loaded uniaxially between the pistons of a powerful press (Anastasiadis et al., 2007; Aydin et al., 2009; Brady and Rowell, 1986; Hadjicontis and Mavromatou, 1994; Hadjicontis et al., 2005; Jouniaux et al., 2006). Rarely have experiments been performed under three-axial loading and, if so, the obtainable information relevant to pre-earthquake signals is necessary limited by the heavy-duty pressure vessels (Lei et al., 2000; Savage et al., 1996).

Rock cylinders, when uniaxially loaded and deformed, will dilate, e.g. bulge outward (Cristescu, 1982), causing tensile stresses in the surface, which lead to microfractures, cracks and failure. The dilatancy concept has been applied to pre-earthquake situations (Scholz, 1978), though it was originally used to describe volume changes during the flow of granular materials (Nedderman, 1992). In realistic earthquake scenarios it is not the rocks at or near the Earth surface that are stressed and fail but the rocks at hypocentral depth, mostly in the 10–35 km range for crustal events. Under high lithostatic overload, microfracturing (if defined as the opening of microcracks) becomes inconceivable. This at once rules out exo-electron emission, which is possible only at solid–gas or solid–vacuum interfaces (Oster et al., 1999). It also rules out other pre-earthquake EM signal generation processes based on the presumed opening of cracks and separation of charges, which lead to emission from X-ray, UV and visible to RF frequencies in unconstrained rock failure experiments (Brady and Rowell, 1986; Brady, 1992).

Similarly, attempts to explain pre-earthquake signals by invoking the piezoelectric and/or piezomagnetic effects run into insurmountable difficulties arising from the fact that piezoelectricity and piezomagnetism are tied to single crystals. The only piezoelectric mineral of rock-forming importance is quartz. Quartz has a screw axis along which a voltage develops when stresses are applied. In any quartz-bearing rock, however, the piezoelectric axes will be randomly oriented, even when the quartz crystals are morphologically aligned. The reason is that quartz occurs with 50:50 probability in left-handed and right-handed varieties where the piezoelectric axes have opposite polarities. As a result, piezovoltages generated in every quartz crystal cancel out, except weakly at the rock surface. Thus, electric dipoles due to the piezoelectric effect cannot build-up in quartz-bearing rocks, even when they are stressed under dynamic load (Ogawa and Utada, 2000a).

The same holds true for the piezomagnetic effect, which is observed in some antiferromagnetic crystals, including minerals such as goethite, FeOOH, and atacamite, $Cu_2Cl(OH)_3$, which are typically found at or near the Earth surface. The only piezomagnetic mineral that occurs as a minor constituent in mafic rocks is pyrrhotite, $Fe_{1-x}S$ (Cullity, 1971). Though individual pyrrhotite crystals will develop a magnetic field when stressed, their random orientation in a rock is bound to cancel out.

In the case of seismo-electric signals (SES) it has been proposed by the Greek group (Varotsos, 2005) that SES signals are generated by transient solid state defects similar to those studied in laboratory experiments (Anastasiadis et al., 2007; Aydin et al., 2009; Kyriazis et al., 2009; Papathanassiou, 2000; Vallianatos and Triantis, 2008). Though pressure-induced electric currents have been described by these authors, their experiments were not set up to recognize that some charge carriers activated by stress might have the capability to flow out of the stressed subvolume and spread far afield. With respect to the mV-level SES signals a clear concept seems to be lacking how such weak dc signals, presumed to be generated in the epicentral area, can be transmitted through the Earth's crust to measuring stations as far as 100 km away. Another group in Greece has long studied electric signals produced during uniaxial compression of rocks (Hadjicontis and Mavromatou, 1994, 1995) and single crystals, including halides such as LiF (Hadjicontis et al., 2005; Hadjicontis et al., 2007).

The electrokinetic effect, widely used to address pre-earthquake signals such as ELF/ULF emissions, leads to streaming potentials when brines are pushed through porous media. Cations are preferentially retained on the walls of the pores, while anions are carried on by the fluid flow. Streaming potentials apply mostly to the top 3–5 km of the crust, where rocks can maintain an open porosity and allow brines to flow even under tectonically stable conditions. Below 5–7 km the lithostatic overload becomes so high that pores tend to close, shutting off most or all fluid flow (Galdin et al., 1986), limiting the development of streaming potentials at greater depths where most crustal earthquakes originate. In addition streaming potentials are very sensitive to the conductivity of the water or saline solution, decreasing rapidly with increasing conductivity. Under realistic shallow crustal conditions they typically reach only a few mV (Darnet and Marquis, 2003). This raises the question whether the electrokinetic effect can generate sufficiently large voltages to account for the reported ELF/ULF emissions.

In the case of the TIR anomalies the explanations offered invoke a diffuse release of CO_2 or radon emanation as prerequisites to the apparent temperature increase. However, there is little or no hard evidence that either of these gases comes out of the Earth surface at fluxes necessary to explain the observed effects. With reference

to radon it has been argued that the alpha particles, which are emitted during radon decay with an energy of nearly 5.5 MeV, produce ~10^5 ions and thus will raise the air ion concentration to such a sufficiently high level to quantitatively explain the TIR anomalies and ionospheric perturbations (Pulinets and Boyarchuk, 2004). This argument does not take into account that, because the alpha particles produce electrons and ions simultaneously in a small air volume, a large fraction recombines near-instantly leading to a much lower number of residual airborne ions. If recombination is factored in, the agreement with the magnitude of the observed TIR anomalies and ionospheric perturbations becomes less favorable.

Apparently the field of pre-earthquake science is in disarray. Almost every reported pre-earthquake phenomenon seems to require a different physical process to arrive at a plausible explanation. Occam's razor states that "entities must not be multiplied beyond necessity", meaning that a simple explanation, if available, tends to be the best (Sober, 1994). Isaac Newton likewise stated "We are to admit no more causes of natural things than such as are both true and sufficient to explain their appearances" (Hawking, 2003).

In this paper I present evidence for a fundamental process in the solid state, long ignored in the geoscience community, which satisfies Occam's razor test and Newton's criterion. It identifies a specific electronic charge carrier, ubiquitous on the majority of crustal rocks, and allows us to address most, if not all reported pre-earthquake phenomena in a unifying way.

The work on which I report here would not have been possible without the help of a number of dedicated collaborators, whose names are listed in the Acknowledgments.

2. Solid state background: positive hole charge carriers

Peroxy links are point defects in fused silica (Ricci et al., 2001), where some of the usual $O_3Si–O–SiO_3$ bonds are replaced by $O_3Si–OO–SiO_3$ links. The same type of peroxy defects exist in the structures of rock-forming minerals, $O_3X–OO–YO_3$ with X, Y = Si^{4+}, Al^{3+}, etc. They are introduced through the incorporation of H_2O into nominally anhydrous minerals that crystallize in H_2O–laden magmas or recrystallize in high-temperature H_2O–laden environments (Freund, 1985). The incorporation of H_2O can be described as splitting of an $O_3SiOSiO_3$ bond, leading to hydroxyls, $O_3Si–OH$, most commonly in pairs. During cooling through the 600–400 °C window, the $O_3Si–OH$ pairs rearrange electronically in such a way that their oxygen (which are in the 2− valence state) donate an electron to their respective protons, H^+, turning them into molecular H_2 molecule and going to the 1− valence state. The two O^- then pair up to form a stable peroxy link:

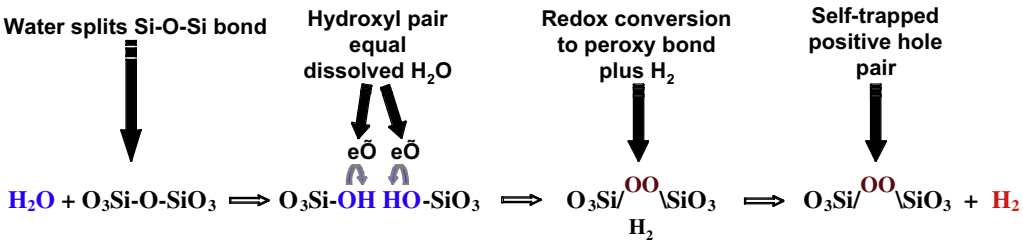

(1)

Every igneous and high-grade metamorphic rock in the Earth's crust, also every sedimentary rock that contains detridal mineral grains from such igneous and high-grade metamorphic rocks, carries a non-zero concentration of peroxy in their constituent minerals. At this point, in order to characterize certain features of the peroxy links, we need to introduce semiconductor terminology.

Ideally, every silicate mineral is made up of O^{2-} anions with metal cations to balance the charge. Any O^- in a mineral structure therefore represents a site, where an electron is missing in the oxygen sublattice. Thus an O^- is a defect electron, also known as a hole. Since this hole exists on the oxygen sublattice, it has been called a positive hole (Griscom, 1990) or phole for short. In a peroxy link two O^- are bonded together forming a very short, but unstable bond. From a semiconductor perspective, a peroxy link is a positive hole pair, PHP. In the PHP the holes are self-trapped and localized. They are electrically inactive.

PHPs are inconspicuous. This is why their ubiquitous presence in minerals and rocks has escaped the attention of researchers for such a long time.

However, there are common processes, which cause the peroxy bonds to break, most significantly the application of deviatoric stresses (Freund et al., 2006). Such stresses cause mineral grains to plastically deform, for instance at grain-to-grain contact points which act as stress concentrators. The deformation is achieved through the movement of dislocations. Each time a dislocation intersects a peroxy link in the mineral matrix, it causes the peroxy bond to break. In this moment an O^{2-} neighboring the peroxy link sends in an electron as outlined in Eq. (2), where an $[SiO_4]^{4-}$ structural unit is taken as the electron donor:

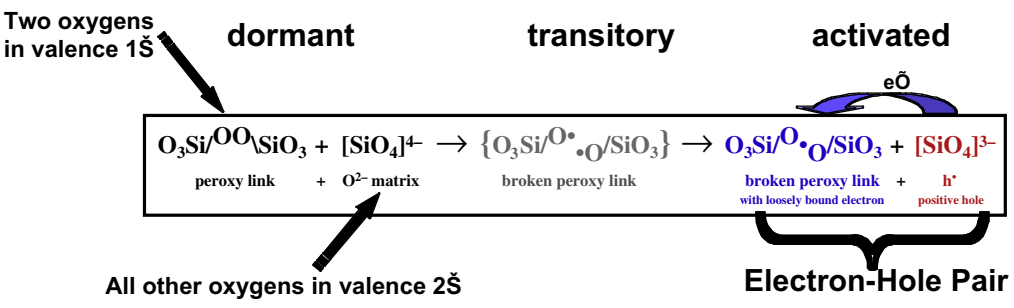

(2)

The broken peroxy link acts as electron receptor. It traps the electron and holds onto it, while the $[SiO_4]^{4-}$, which had donated the electron, thereby turns into a positive hole, symbolized by $h^{\cdot}$.

The $h^{\cdot}$ is an electronic state associated with a missing electron in the O^{2-} sublattice. It has no physical reality except that it is a wavefunction associated with an O^{2-} site where an electron is missing. At the same time the $h^{\cdot}$ is an electronic charge carrier, which resides in the valence band of otherwise insulating mineral grains. Even though silicate minerals are insulators when it comes to allowing electrons to pass through, they are p-type semiconductors when it comes to positive holes and their propagation through the mineral structure.

Indeed, all mineral grains that contain positive holes provide energy levels at the upper edge of their valence bands along which $h^{\cdot}$ can propagate. In addition we note that the valence bands of all mineral grains in a given rock are electrically connected. We can therefore expect the $h^{\cdot}$ to not only propagate through individual mineral grains but also to cross grain boundaries, e.g. propagate from grain to grain wherever grains are in physical contact. This holds true also for mineral grains cemented together or separated by alteration products

Positive holes are highly mobile charge carriers. They are thought to propagate as depicted in Eq. (3) by electrons hopping from O^{2-} to O^{-} opposite to the direction of the propagating $h^{\cdot}$:

$$\begin{array}{ccccccccccccccccccc}
- & - & \leftarrow & e' & - & - & - & \Leftrightarrow & - & - & - & \leftarrow & e' & - & - & \Leftrightarrow & - & - & - & - & \leftarrow & e' & - \\
O^{2-} & O^{2-} & \mathbf{O^{-}} & O^{2-} & O^{2-} & O^{2-} & O^{2-} & \Leftrightarrow & O^{2-} & O^{2-} & O^{2-} & \mathbf{O^{-}} & O^{2-} & O^{2-} & O^{2-} & \Leftrightarrow & O^{2-} & O^{2-} & O^{2-} & O^{2-} & \mathbf{O^{-}} & O^{2-} & O^{2-} \\
- & - & h^{\bullet} & \rightarrow & - & - & - & \Leftrightarrow & - & - & - & h^{\bullet} & \rightarrow & - & - & \Leftrightarrow & - & - & - & - & h^{\bullet} & \rightarrow & -
\end{array} \quad (3)$$

If the electrons hop at the frequency of thermal phonons, about 10^{12} Hz, and if, with every hop, the $h^{\cdot}$ advance by 2.8 Å (the average O^{2-}–O^{2-} distance, 2.8×10^{-10} m), the phase velocity, e.g. the maximum speed with which an $h^{\cdot}$ pulse can propagate, would be on the order of 280 m s^{-1}. The measured phase velocity of $h^{\cdot}$ charge clouds spreading through various rocks, 200–300 m s^{-1} (Freund, 2002; Hollerman et al., 2006), is consistent with such a mechanism involving phonon-assisted electron hopping (Shluger et al., 1992). The drift velocity of an actual $h^{\cdot}$ wave traveling along its self-generated electric field gradient will be significantly lower.

As stated above, the $h^{\cdot}$ charge carriers travel along the upper edge of the valence band. However, for $h^{\cdot}$ to propagate, the mineral grains or rocks must have a pre-existing p-type conductivity, e.g. a non-zero concentration of defect electrons in the oxygen sublattice. Only when this condition is fulfilled can $h^{\cdot}$ charge carriers move through the mineral matrix and, ultimately, through the rock. In other words, rocks must contain a non-zero concentration of $h^{\cdot}$, already in the unstressed state. Rocks, which do not provide at least some $h^{\cdot}$-based electrical conductivity, will not be able to conduct $h^{\cdot}$.

Fig. 1a shows the electrical conductivity s of typical igneous rocks over the temperature range typical of the Earth's continental crust down to 30–35 km, here plotted as $\log \sigma$ versus $1/T$ (K) (Parkhomenko and Bondarenko, 1986). Fig. 1b shows the electrical conductivity s of nominally high purity MgO single crystals, used to fully characterize $h^{\cdot}$ charge carriers and their temperature-dependent behavior (Freund et al., 1993; Kathrein and Freund, 1983). The electrical conductivity response was measured during a combined heating–cooling program designed to demonstrate the thermal activation of $h^{\cdot}$ charge carriers and their characteristic 1 eV activation energy. It is remarkable that the electrical conductivity of igneous and high-grade metamorphic rocks is marked by the same activation energy, $E_{act} \approx 1$ eV, as that of MgO single crystals. This is a sign of the omnipresence of $h^{\cdot}$ charge carriers. While heating leads to the activation of $h^{\cdot}$ charge carriers, there are other $h^{\cdot}$ activation processes as well, most prominently the application of stress.

3. Expected observables

3.1. Flow of positive hole charge carriers through the bulk

Application of deviatoric stress such as during uniaxial loading, causes dislocations to move and new dislocations to be generated in response to the shear forces acting on mineral grains. The moving dislocations activate $h^{\cdot}$ charge carriers alongside electrons e'. Stressing creates a high concentration of $h^{\cdot}$ and e' in the stressed subvolume as outlined in Fig. 2. The $h^{\cdot}$ are mobile. They are capable of spreading out into the unstressed rock volume following the concentration gradient. By contrast, the e' remain trapped at the sites of the broken peroxy bonds. They cannot spread out (Freund, 2002; Freund et al., 2006).

The situation depicted in Fig. 2 resembles that in an electrochemical battery. In the case of an electrochemical battery the positive charges in the anodic subvolume are metal cations, capable of spreading into the electrolyte and of carrying a current. The electrons cannot enter the electrolyte, but can pass from the anodic subvolume into a metal contact, the "anode". From there they could pass to the cathode to close the battery circuit, if an appropriate pathway is made available.

In the case of a rock battery, the stressed rock becomes the anodic subvolume from where positive charges can flow out. The fundamental difference is that the charge carriers in the rocks are not cations but positive holes, $h^{\cdot}$. The anodic subvolume is not chemically different but physically different, through the level of stress.

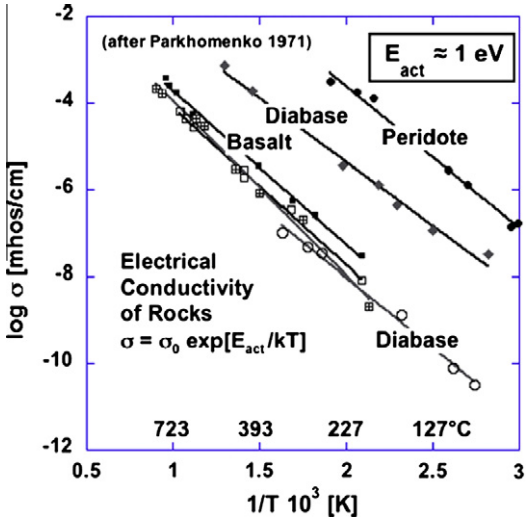

Fig. 1a. Selection of $\log \sigma$ versus $1/T$ (K) plots of different mafic and ultramafic rocks to illustrate the common 1 eV activation energy for their electrical conductivity response (after Parkhomenko and Bondarenko (1986)).

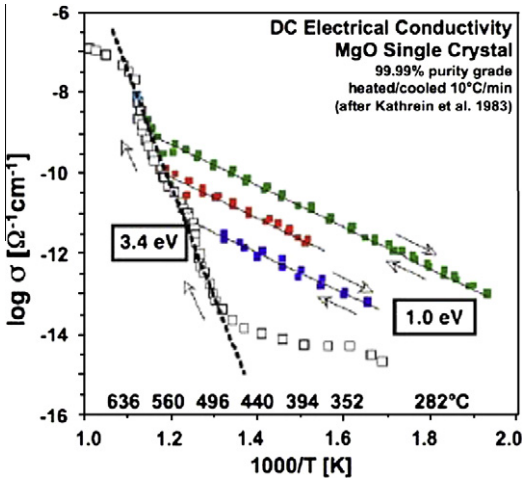

Fig. 1b. Electrical conductivity of single crystal MgO during heating dominated by the thermal activation of h$^{\cdot}$ charge carriers with a characteristic 1 eV activation energy (after Kathrein and Freund (1983)).

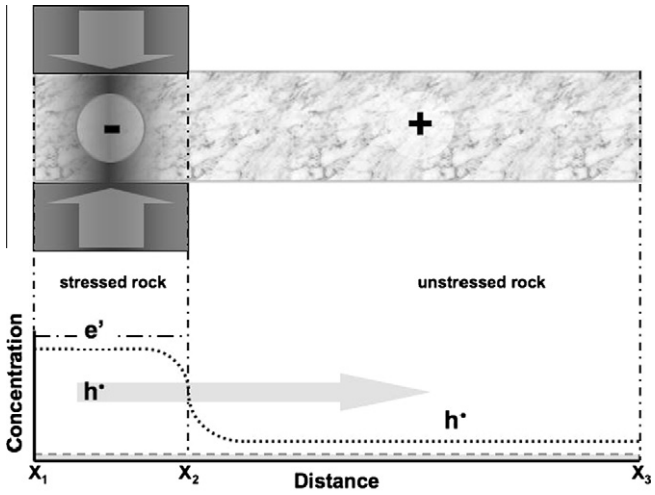

Fig. 2. Set-up to demonstrate the activation of positive holes, which flow out of the stressed rock volume. Bottom: before application of stress the h$^{\cdot}$ concentration is uniform and low (dashed line). After application of stress the concentration of e′ and h$^{\cdot}$ increases in the stressed subvolume (dot-dashed). The h$^{\cdot}$ flow out causing the unstressed rock to become positively charged relative to the stressed rock. The dotted line gives schematically the h$^{\cdot}$ concentration profile.

To "charge" the rock battery work needs to be done. This work is not chemical but mechanical, provided by the application of deviatoric stress.

The h$^{\cdot}$ outflow from the stressed rock subvolume has two immediate consequences:

(i) it sets up a potential difference, which causes the unstressed rock to become positively charged relative to the stressed rock. The potential difference creates an electric field, which counteracts the h$^{\cdot}$ outflow and will eventually stop it.
(ii) since the h$^{\cdot}$ charge carriers inside the unstressed rock repel each other electrostatically, they will be pushed toward the surface and produce a positive surface charge.

The build-up of a surface charge can be followed experimentally with a set-up as depicted in Figs. 3a and 3b using a non-contact capacitive sensor to measure the potential difference between

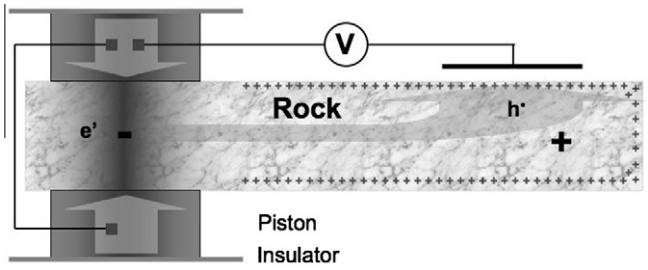

Fig. 3a. Set-up to measure the positive surface potential, due to h$^{\cdot}$, on a flat rock surface with a non-contact capacitive sensor.

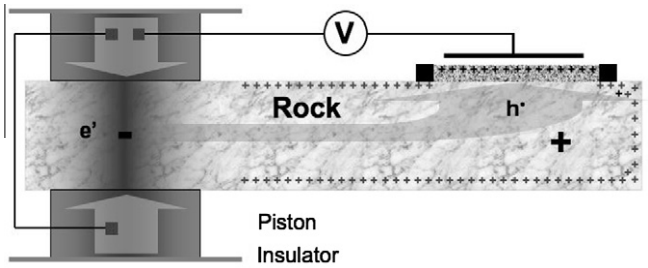

Fig. 3b. Demonstration that the h$^{\cdot}$ propagate through sand/soil building up a positive charge layer on the surface of the sand or soil (stippled).

the unstressed rock and the pistons. The pistons must be electrically insulated from ground. Fig. 3a shows the configuration to obtain the surface potential off the bare rock surface. Fig. 3b shows the configuration to obtain the surface potential off a sand or soil surface on top of the rock.

The battery circuit can be completed by placing a Cu contact on the surface of the unstressed rock as shown in Fig. 4a. Replacing the voltmeter with an ammeter allows us to measure the battery current. The Cu contact acts as cathode. By pressing a Cu contact on a layer of sand or soil as in Fig. 4b it can be demonstrated that

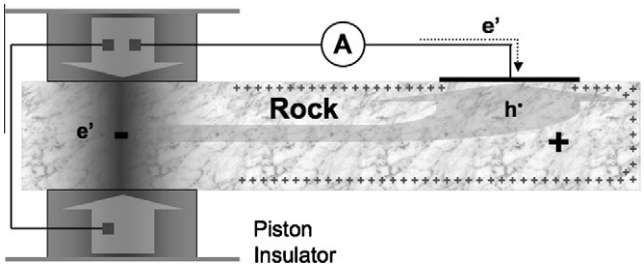

Fig. 4a. Set-up to measure the battery current with a Cu contact placed directly on the rock.

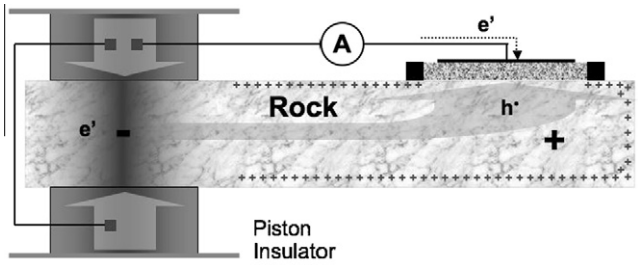

Fig. 4b. Demonstration that the h$^{\cdot}$ current also flows through sand and/or soil (stippled).

the battery current that flows through the rock will also flow through sand and soil, even moist sand and soil. This is consistent with the information provided above that the $h^{\cdot}$ propagate by using energy levels at the upper edge of the valence band. Since the valence bands of all mineral grains that are in contact are electrically connected, the $h^{\cdot}$ charge carriers are expected to be able to cross from grain to grain. They can flow from grain to grain in loosely consolidated sand and soil.

3.2. Expected reactions at the rock–air interface

The accumulation of positive hole charge carriers at the surface leads not only to a surface charge layer but also to an electric field. In fact there at two electric fields to be considered: one that is exterior to the rock surface and one that is essentially a subsurface electric field caused by the accumulation of the charge carriers in the top layers of the solid. The exterior field is amenable to measurement by a capacitive sensor as depicted in Fig. 3a and 3b.

The subsurface charge distribution, the electric potential and associated electric field can be calculated using Schottky barrier theory. Fig. 5 shows an example of the potential and electric field calculated for the flat surface of a dielectric medium with a dielectric constant $\varepsilon = 10$ assumed to contain 10^{17} and 10^{18} mobile positive charges per cm^3, equivalent to 10 and 100 ppm respectively, but no mobile negative charges (King and Freund, 1984).

The electric potential at the surface is +400 mV relative to the bulk from where the positive charges came. The surface potential is independent of the charge carrier concentration. However, because driving force for the charge carrier accumulation at the surface is their mutual electrostatic repulsion in the bulk, their density in the subsurface layer and the associated electric fields E, increase rapidly with increasing charge carrier concentration. Under the conditions chosen here, the flat surface value for a charge carrier concentration of 100 ppm reaches 400,000 V cm^{-1}. At corners, edges and any point with small radii the E values will be significantly higher. The electric fields can therefore be expected to reach and exceed the ionization threshold of air.

To test this prediction in the laboratory we can modify the set-up in Fig. 3a and 3b by applying a bias voltage to the metal plate above the rock surface, which thereby becomes an ion collector, and by replacing the voltmeter with an ammeter.

If air molecules become field-ionized as depicted in Fig. 6a, they loose an electron to the rock surface and turn into airborne positive ions. Such positive airborne ions would produce an electric current between the rock surface and the negatively bias ion collector plate.

If the electric fields at the rock surface increase further, it is conceivable that they would accelerate electrons to energies sufficiently large to impact-ionize neutral gas molecules. This in turn would lead to ionization avalanches, triggering corona discharges as reported earlier (Freund, 2002). Corona discharges produce free electrons plus a mixture of positive and negative airborne ions. To measure these processes we apply a positive bias to the ion collector plate as depicted in Fig. 6b.

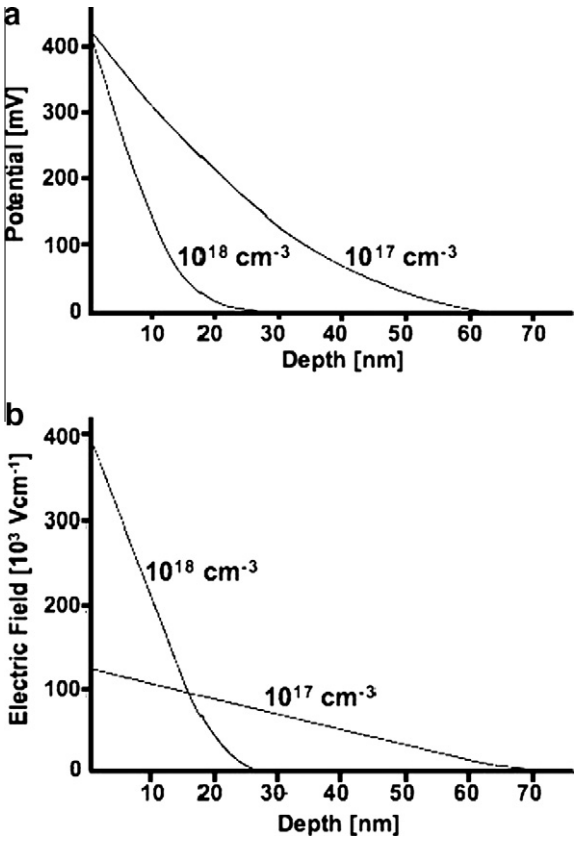

Fig. 5. Surface potential and subsurface electric fields calculated for a flat surface of a dielectric medium with a dielectric constant of 10 and two charge carrier concentrations, 10 and 100 ppm (after King and Freund (1984)).

4. Laboratory validation

4.1. Currents flowing through the bulk of the rocks

An expedient way to demonstrate the rock battery is to apply Cu contacts with a graphite-loaded conductive adhesive to both ends of a slab of a rock, run a wire through an ammeter, and stress one end (Freund et al., 2006). Fig. 7a shows the current generated when a slab of granite, 4 m long, $20 \times 20\ cm^2$ cross section is loaded between two round pistons, 20 cm diameter, insulated from the press. The load was increased within 5 min from 0 to 60,000 lbs, equivalent to about 20 MPa, 10% of the fracture strength, held constant for 5 min and unloaded over 5 min. The battery current began to flow immediately upon loading and increased rapidly. At less than 5% fracture strength the current

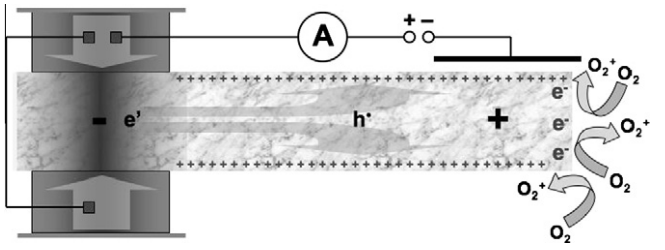

Fig. 6a. Set-up to measure the field ionization of air molecules leading to airborne positive ions.

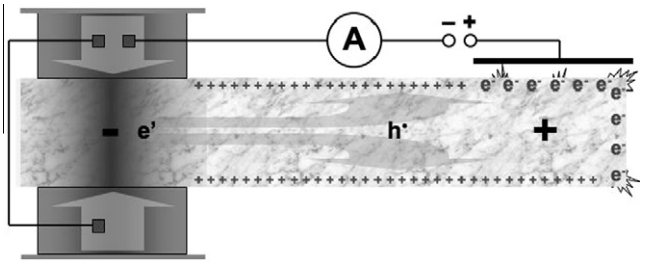

Fig. 6b. Set-up to measure free electrons and negative airborne ions during corona discharges.

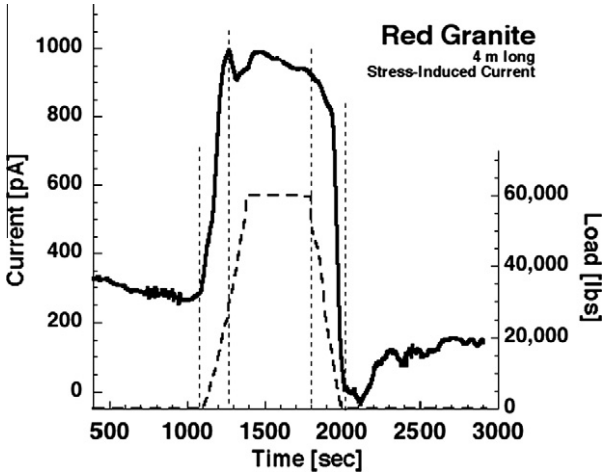

Fig. 7a. Current versus time upon loading/unloading granite a 4 m long granite.

reached a maximum around 1 nA, went through a brief maximum–minimum sequence, and stayed high under constant load, decreasing slowly. Upon unloading to below 5% fracture strength current decayed rapidly and returned to the slowly decreasing background after some time.

The current that flows through the rock is limited by the internal resistance *R*, which is constant at constant temperature *T*. The self-generated battery V is a function of the rate of loading and found to be higher at high stress rates (Takeuchi et al., 2006). The reason is that, during stressing, different types of $h^{\cdot}$ charge carriers are activated, characterized by different decay times. Short-lived $h^{\cdot}$ appear and disappear during rapid loading. Some $h^{\cdot}$ remain active only for seconds or minutes, others for longer. This behavior is illustrated in Fig. 7b, showing the outflow of current from a 10 cm^3 rock volume at the center of a $30 \times 30 \times 0.9$ cm^3 gabbro tile, loaded within 5 s from 0 to a constant stress level of 48 MPa, approximately 20% of the fracture strength of this rock. On the scale of this plot the current starts around 250 pA and decays over the course of 10 h, here shown as log *I* versus time *t*. The three straight sections suggest the activation of three types of $h^{\cdot}$ charge carriers with different lifetimes increasing from a few hours to several days. Long-term experiments have indicated that some $h^{\cdot}$ charge carriers remain active for more than 2½ months provided the stress level on the rock is maintained or increased. Results from fast loading experiments,

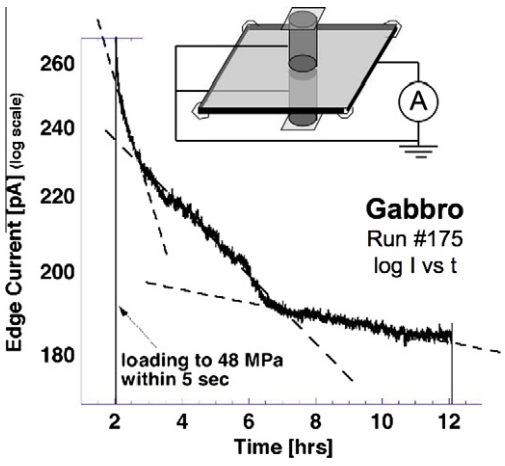

Fig. 7b. Outflow current a stressed gabbro tile over 10 h at constant load (48 MPa).

up to 20 MPa s^{-1} from 0 to 48 MPa, indicate that shorter-lived $h^{\cdot}$ charge carriers are activated under these conditions, which give rise to initial voltage pulses and brief current pulses up to 100× stronger as the currents shown in Fig. 7b.

Understanding whether and how currents can flow through rocks at depth is intimately linked to the question of EM emissions, in particular ELF/ULF emissions coming from deep below. From the perspective of $h^{\cdot}$ currents one prerequisite is battery circuit closure. The reason is that, if $h^{\cdot}$ charge carriers flow out of a stressed rock subvolume deep in the Earth's crust and spread into the surrounding unstressed rocks without circuit closure, the build-up of the battery voltage will soon put an end to the $h^{\cdot}$ outflow. Therefore, as long as the battery circuit is not closed, allowing for a return current of equal magnitude, the $h^{\cdot}$ outflow current can only be transient and weak. Any persisting stress-activated $h^{\cdot}$ current requires a process that allows the electrons, which are co-activated in the stressed rock volume, to follow suit and also flow out. Somewhere along their path they must recombine with the $h^{\cdot}$ charge carriers to establish a closed current loop.

In the laboratory it is easy to close the battery circuit. As depicted in Figs. 4a and 4b, we do it by running a metal wire from the pistons or a Cu contact on the stressed rock volume (acting as anode) to a Cu contact on the unstressed portion of the rock (acting as cathode). The $h^{\cdot}$ charge carriers traveling through the rock will then recombine with the electrons traveling through the metal wire.

In the field, in the Earth's crust, closure of the battery circuit is more difficult to achieve. Three possible scenarios have been identified:

(i) Circuit closure is achieved by electrons in the stressed rock volume flowing downward in the crust to reach the postulated boundary where, at a temperature of about 500 °C, equivalent to about 30–35 km depth, the rocks turn from a p-type semiconducting state to an n-type state, e.g. where rocks are hot enough to be able to conduct electrons (Freund, 2007a,b).

(ii) Circuit closure is achieved by $h^{\cdot}$ charge carriers encountering a rock–water interface where they convert H_2O to H_2O_2, while the actual current continues to flow due to the electrolytical conductivity of water, in particular of saline water. If the local conditions are such that an electrolytically conductive path exists, which connect back to the stressed rock volume, circuit closure can conceivably be achieved via this mechanism (Freund, 2009).

(iii) Circuit closure is achieved by currents flowing through the air, when massive air ionization takes place at the rock-air or ground-air interface as will be discussed in Section 5.2.

While space does not permit addressing the circuit closure condition (ii), I would like to comment on the observation that ULF, MHz and kHz EM emissions tend to appear one after the other, both on the laboratory and the geophysical scale. The lead time for ULF signals sometimes extends up to a few months before the earthquake, whereas EM emissions in the kHz to MHz range tend to be observed during the last few days to few hours before an event. This seems to suggest that the EM signals spanning this wide frequency range arise from different mechanisms during consecutive stages of the earthquake preparation process.

Different physical mechanisms may not be necessary. During our laboratory experiments we notice that $h^{\cdot}$ outflow currents seldom flow smoothly. They tend to fluctuate, occasionally with large amplitudes, indicating instabilities or some coupling mechanisms. Since the frequency of any EM emissions is given by the time derivative of the current, slowly changing $h^{\cdot}$ currents will produce low

to ultralow frequency EM emissions. Fast changing $h^{\cdot}$ currents will lead to higher frequency EM emissions.

One recurring type of fluctuations, which we observe in laboratory experiments, is clearly related to the stress rate and activation of $h^{\cdot}$ with different lifetimes. So far we have identified at least three families of $h^{\cdot}$ charge carriers in gabbro with distinct lifetimes as short as 1 s to as long as 12–24 h (Freund, 2009). Depending how fast we apply stress, the $h^{\cdot}$ current versus time curves change in a reproducible way. When the applied stress rates are small, the $h^{\cdot}$ currents increase moderately fast, though not linearly with time. When the applied stress rates are high, a sharp initial peak appears with a half width of about 1 s caused by the activation of $h^{\cdot}$ carriers, which live only long enough to produce a short current pulse.

We can cautiously apply these observations to realistic earthquake situations where the stresses, which build-up around the hypocenter at depth, accelerate as the time of failure approaches. The reason for the accelerating stress is that the speed, with which sections of plates are pushed against each other by tectonic forces, is constant, at least on the time scales of interest here. When two brittle materials are pushed against each other at constant velocity but under large overload, they have no possibility to dilate. Since the compressibility is a steep function of distance (Vinet et al., 1987), the stresses build-up nonlinearly, probably along an exponential curve, until the critical point of rupture is reached (Main, 1996; Sornette and Sornette, 1990).

On the basis of the foregoing description of our $h^{\cdot}$ current measurements at different stress rates we can expect an $h^{\cdot}$ current outflow from the maximally stressed volume that increases with time, provided the battery circuit is closed. If these currents fluctuate as they often do under laboratory conditions, we would indeed expect to see EM emissions starting in the ULF/ELF range and evolving toward higher frequencies as the time of the earthquake draws nearer. This can – at least conceptually – explain the above-mentioned field observations of ever higher frequency EM emissions evolving with time without having to invoke different generation mechanisms.

However, there is still a need to consider additional mechanisms for the emission of kHz and MHz signals. The reason is that, while ULF/ELF waves are only weakly attenuated in the crust and may be able to travel upward from hypocentral depth to the surface of the Earth, higher frequency EM waves are strongly absorbed. For them to be detectable at the surface of the Earth they must be generated at or near the surface. Processes that could provide the necessary mechanism will be discussed in the next section.

4.2. Charge carriers arriving at the surface

Many reported pre-earthquake signals point to processes taking place at the Earth surface. These phenomena include

(i) Changes in the atmosphere,
(ii) Perturbations in the ionosphere,
(iii) Luminous phenomena, often called earthquake lights,
(iv) Unusual animal behavior,
(v) Enhanced infrared emission from around the epicentral region seen in satellite images.

As indicated above and illustrated in Figs. 3a and 3b positive hole charge carriers, once stress-activated, have a strong tendency to be pushed to the surface and form distinct surface/subsurface charge layers. What is true for laboratory-sized samples should also be true on the larger scales for processes that involve the propagation of $h^{\cdot}$ through the Earth's crust and their arrival at the Earth's surface.

Standard theoretical methods developed to deal with charge boundary layers in Schottky diodes allow us to calculate the electric fields associated with surface charge layers (King and Freund, 1984). Though very steep these electric fields are not macroscopic. They are microscopic electric fields at the surface and extending into the solid on the nanometer scale. As shown in the example given in Fig. 5, these fields can have high values even at moderate charge carrier concentrations in the bulk and for an atomically flat surface. At corners and edges, in fact at any topographic high points, where $h^{\cdot}$ will accumulate in higher concentrations, these fields are expected to easily exceed the ionization threshold of air, typically 2×10^6 V cm^{-1} (Manna and Chakrabarti, 1987).

Since there is clear experimental evidence that positive holes are capable of diffusing not only through compact rocks but also through sand and soil, there is little doubt that $h^{\cdot}$ charge carriers, activated by tectonic stresses at depth, will be capable of migrating to the Earth surface. They are expected to produce electric fields at the ground-to-air interface similarly steep compared to those measured in laboratory experiments. The question is whether these surface fields lead to follow-on processes, which help understand the multitude of reported pre-earthquake signals.

Surface potentials can be measured with a capacitive sensor as sketched in Figs. 3a and 3b (Takeuchi et al., 2006). Fig. 8 shows how the surface potential evolves during loading of a block of gabbro up to failure. The measurement was conducted inside a Faraday cage on a $30 \times 15 \times 10$ cm^3 piece of gabbro loaded at one end using steel pistons with hardened "teeth", acting as stress concentrators to be able to stress the rock to the breaking point with relatively modest loads on the order of 45,000 lbs, about 20 tons (Freund et al., 2009).

The surface potential is extremely sensitive to very slight mechanical stresses acting on the rock by, for instance, the platen of the hydraulic press inching upward at the beginning of the run (dashed section of the curve). Immediately thereafter, as the load is applied, the surface potential increases rapidly to about +3 V (significantly higher than the 0.4 V shown in Fig. 5). While the load increases further, the surface potential fluctuates. The smooth

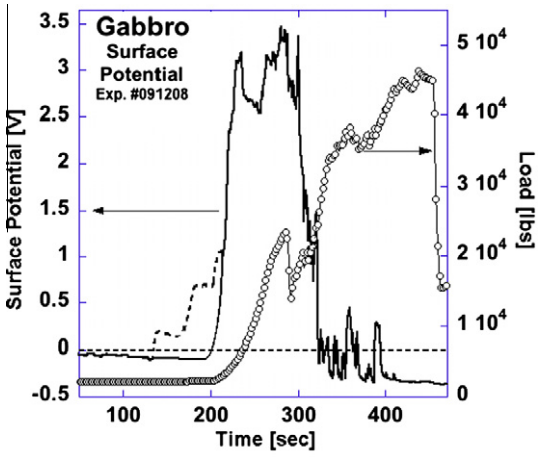

Fig. 8. Evolution of the surface potential (solid line, left ordinate) of a block of gabbro loaded at the far end at an approximately constant rate in a hydraulic press using pistons with hardened steel bearings as stress concentrators (open circles, right ordinate). Massive deformation on a local scale occurs when the steel bearings "sink" into the rock causing a temporary drop in the hydraulic fluid pressure and eventual failure (at the 460 s mark). Because of the use of stress concentrators we give the load (in lbs), not the stress (in MPa). Based on prior tests it is known that, immediately upon loading, a robust positive surface potential builds up (solid line). It quickly increases to about +3 V, fluctuates and collapses suddenly reversing to weakly negative values with continuing fluctuations. (Dotted line: initial surface charges as measured caused by ever to slight mechanical forces acting on the rock prior to stressing.)

loading curve is interrupted by periods where the "teeth" sink into the rock. Close to ½ the fracture load, the positive surface potential suddenly collapses and turns negative, while continuing to fluctuate until the rock failed.

The initial increase of the surface potential to around +3 V can be readily understood by assuming that $h^{\cdot}$ charge carriers flow out of the stressed rock into the unstressed rock, generating a positive surface/subsurface charge layer as discussed in Section 2.2. Obviously other processes come into play that cause the positive surface potential to fluctuate, then collapse and turn negative.

Using the same basic set-up – a Faraday cage and pistons "with teeth" to load $30 \times 15 \times 10\ cm^3$ blocks of gabbro – a negative or positive bias applied to the capacitive sensor turns it into an ion collector for airborne positive and negative ions, respectively. Figs. 9a and 9b show typical results.

Under negative bias, in Fig. 9a, there is at first no ion current between the rock surface and the ion collector plate. When the load reaches a level where the surface potential has already increased to values around +3 V and begins to fluctuate, an ion current starts to flow. The ion current comes in pulses, which are often correlated with moments when the "teeth" sink into the rock causing massive local deformation. At other times, while the load increases smoothly, pulses of positive ions flow between the rock surface and the ion collector plate. Typically, when the load is greater than approximately ½ that required to cause fracture, the positive ion current rises continuously overlain by pulses.

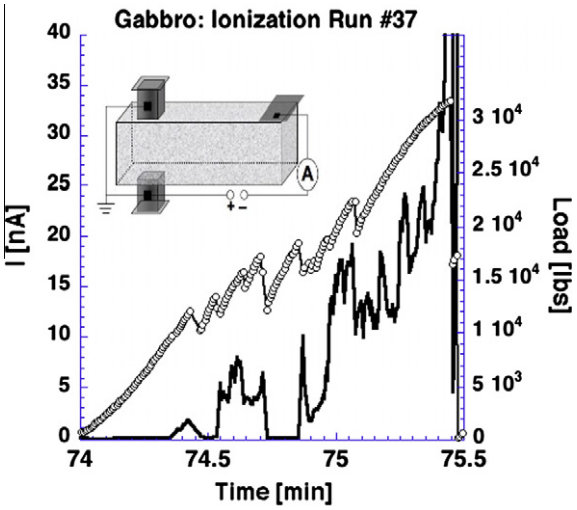

Fig. 9a. Generation of positive airborne ions upon loading a gabbro ($10 \times 15 \times 30\ cm^3$) at the far end as described for Fig. 8. Inset: set-up with ion collector 5 mm above rock.

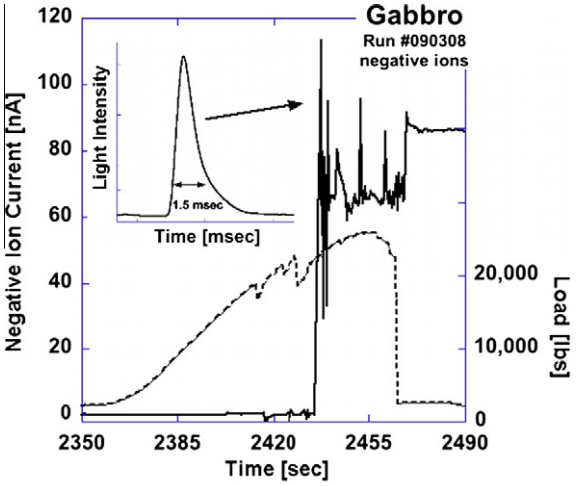

Fig. 9b. Generation of negative airborne ions and electrons upon loading a gabbro ($10 \times 15 \times 30\ cm^3$) at the far end. Inset: photodiode signal of light flash.

Under positive bias, in Fig. 9b, no current flows across the air gap until close to or beyond the ½ mark to fracture. The on-set usually comes in a sudden burst followed by more spikes, each accompanied by a flash of visible light (measured by a photodiode), lasting for 1–2 ms. The sharp on-set is followed by a continuous, elevated current flowing through the 5 mm air gap with superimposed current spikes.

These experiments show that, during loading, air becomes ionized at the rock surface. While the positive surface potential starts to build-up immediately upon loading as depicted in Fig. 8, the ionization of the air does not start until the load has reached a level sufficient to produce a surface potential on the order of +3 V. At first only positive airborne ions are formed, indicating that field-ionization takes place. If air molecules approach the rock surface close enough to "feel" the steep subsurface electric field depicted in Fig. 5b, they become so strongly polarized that they lose an electron to the rock surface and become airborne positive ions. Given the area of the ion collector plate ($10 \times 20\ cm^2$) the ion currents of 10–20 nA flowing through the air gap indicate that rate of formation of positive airborne ions in these experiments is on the order of $10^9\ cm^{-2}\ s^{-1}$.

At still higher loads, typically >1/2 to failure, a different process sets in. Suddenly corona discharges occur, probably emitted from corners and edges of the rock (Freund, 2002). Such corona discharges indicate that the positive surface field has reached a point where it can accelerate free electrons to kinetic energies that are sufficiently high to impact-ionize neutral gas molecules. Such electrons always exist in small concentrations in the ambient air due to cosmic rays or radon decay. However, once such an electron is accelerated to the point of ionizing air molecules by impact, it can trigger an avalanche, which generates a highly ionized plasma characteristic of a corona discharge. The free electrons, now abundantly produced by the discharges, rain down onto the rock surface. They cause the positive surface potential to collapse as illustrated in Fig. 8 and to abruptly change from distinctly positive (around +3 V) to weakly negative (around +400 mV). The collapse of the positive surface potential turns off the corona discharge near-instantly. However, due to the continuing flow of $h^{\cdot}$ charge carriers from the bulk to the surface, the process restarts quickly, causing rapid surface potential fluctuations and rapid-fire sequences of corona discharges. Under these conditions production rates of positive and negative airborne ions in excess of $10^{10}\ cm^{-2}\ s^{-1}$ have been measured (Freund et al., 2009).

5. Correlation with field observations

5.1. Air ionization at the ground-to-air interface

Normally, under "fair weather conditions", the rates at which air molecules are ionized at sea level are on the order of 20–200 $cm^{-3}\ s^{-1}$ (Gringel et al., 1986). Increased air ionization at the ground-to-air interface has long been discussed in the context of pre-earthquake phenomena (Omori et al., 2009; Pulinets, 2007). A rise in air conductivity is thought to influence in characteristic ways processes such as cloud formation (Guo and Wang, 2008; Pulinets et al., 2006), ionospheric perturbations (Chen et al., 1999; Hayakawa et al., 2005; Hayakawa, 2007; Liperovsky et al., 2000; Pulinets, 2007; Sorokin et al., 2006; Zakharenkova

et al., 2007), thermal infrared anomalies (Ouzounov and Freund, 2004; Ouzounov et al., 2006; Qiang et al., 1999; Saraf et al., 2008; Singh, 2008; Tramutoli et al., 2005; Tronin, 2000b; Tronin et al., 2004), and other phenomena that might be indicators for impending seismic activity. The unanswered question was: if these transient increases in air conductivity are real and linked to the build-up of tectonic stresses below, what is the underlying physical process?

Until now two explanations have been offered, both based on the concept that the build-up of stress in the hypocentral region will lead to stresses in a halo surrounding the hypocenter and cause microfracturing. The first explanation invokes the stresses necessary to cause microfractures and assumes that these stresses would lead to locally high voltages due to the piezoelectricity of quartz crystals, hence, to ionization of air. The second considers the opening of cracks during microfracturing as a mechanism to allow radon to escape from the ground and to ionize the air.

The concept of microfracturing supposed to affect a large region around the future hypocenter is a variant of the dilatancy model proposed in the 1960s (Brace et al., 1966). Dilatancy has been used for some time to explain data from laboratory and field studies (Brace, 1975; Dobrovolsky et al., 1979; Hadley, 1975; Nur, 1974) but has been effectively abandoned in recent years in the light of the fact that there is no evidence for the build-up of sufficiently high stresses to cause microfracturing far from the hypocenter (Johnston, 1997; Scholz, 2002). The concept that stressed quartz crystals in rocks might produce piezoelectric voltages of sufficient strength to cause air ionization (Bishop, 1981; Tuck et al., 1977) is also not well supported despite extensive modeling efforts (Ogawa and Utada, 2000b).

The idea that radon gas would emanate from the ground in large quantities to significantly ionize the air has been widely used to explain pre-earthquake ionospheric perturbations (Ondoh, 2003; Oyama et al., 2008; Pulinets, 2007, 2009) and thermal IR anomalies (Ouzounov et al., 2006; Qiang et al., 1991; Tronin, 2002; Tronin et al., 2004; Xu et al., 1991). The scenario that is generally envisioned can be described as follows: As stresses in the hypocentral region build-up, a halo of pervasive microfracturing spreads outward through the crust, allowing radon gas trapped in uranium- and radium-bearing rocks to escape and percolate upward through rocks and soil. The radioactive decay of the ^{222}Ra atoms will cause the formation of about 10^5 ions cm^{-3} and, hence, an increase in air conductivity. The radius r of the so-called "earthquake preparation zone", where microfracturing will occur is thought to scale with the magnitude M of the impending earthquake as $r = 10^{0.43M}$ km (Dobrovolsky et al., 1979). This implies that the diameter of the "preparation zone" for an $M = 5$ seismic event would extend over 100–200 km and be significantly larger for more powerful earthquakes. The ionospheric perturbations are explained by the effect that an increased air conductivity in the lower atmosphere over such a wide region would have on the ionosphere and on the vertical distribution of electrons and ions in the ionospheric plasma.

Similarly, with respect to pre-earthquake "thermal anomalies", radon emanation from the ground and concomitant ionization of the air are thought to lead to condensation of water vapor on the airborne ions and to the release of latent heat of condensation. This would heat up the air and cause the "thermal anomalies" reported from night-time infrared satellite images (Ouzounov et al., 2006; Qiang et al., 1991; Tronin, 2002; Tronin et al., 2004; Xu et al., 1991).

Fig. 10 shows the rate of airborne ionizations under "fair weather conditions" in the lower 10 km of the atmosphere (Gringel et al., 1986; Hoppel et al., 1986). The contribution from cosmic rays is near-constant below 1000 m, amounting to ~2 ions cm^{-3} s^{-1}. The contribution from backscattered beta and gamma rays and ionizing

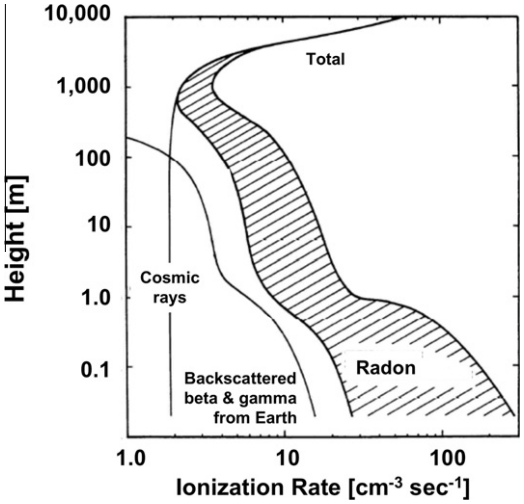

Fig. 10. Rate of air ionization in the first 10 km of the atmosphere under "fair weather" conditions (after Gringel et al. (1986)).

radiation from radioactive decays in the Earth, except radon, is on the order of 20 ion cm^{-3} s^{-1} at the surface, decreasing to nil in the first 100–200 m. The contribution from radon varies typically from ~30 ions cm^{-3} s^{-1} to barely 300 ions cm^{-3} s^{-1} at the Earth's surface and decreases to less than 5 ions cm^{-3} s^{-1} within the first 1000 m.

Field data near the Earth surface or in shallow holes indicate that, prior to seismic activity within a radius up to about 100 km, the radon concentrations can increase by a factor up to 10 over periods of days to months and decrease again after the seismic activity has subsided (Chyi et al., 2002; İnan et al., 2008; Nagarajaa et al., 2003; Tsvetkova et al., 2001). Occasionally the radon concentrations increase by not more than 20–30% above longtime background values (Yasuoka et al., 2009). In some cases radon variations are found to be narrowly constrained to active sections of a fault on the scale of tens of meters (King, 1980).

5.2. Reports on massive air ionization

At the same time, there are reports of massive air ionization events reaching up to 10^5 ions cm^{-3}, typically lasting from a few hours to up to 2 days, posted on the website of the Japanese PISCO ground station network (Hattori et al., 2008; Wasa and Wadatsumi, 2003). The airborne ions are positive, sometimes exclusively positive, at other times both positive and negative. Unfortunately, due to patent interests (Inubushi and Hiroyuki, 2005), the full data are not made publicly available. However, plots presented on the website suggests that the airborne ion concentrations are often 2–3 orders of magnitudes higher than those, which can reasonably be associated with changes in the radon emanation from the ground. The areas with episodes of high levels of air ionization extend over tens, possibly hundreds of kilometers. If such dramatic increases in regional air ionization were due to emanation of radioactive radon from the ground, it would clearly represent a major public health issue (Smith et al., 2007; Suess, 2004).

An episode of strongly increased air conductivity was also observed in California during the lead-up to the $M = 5.4$ Alum Rock earthquake of October 30, 2007. In the weeks prior to this event an air conductivity sensor at one of the CalMagNet stations situated only 2 km from the epicenter recorded short pulses. About 20 h before the earthquake, a sustained period of massive air ionization saturated the sensor for over 13 h (Bleier et al., 2009). Simultaneously, an identical air conductivity sensor at another Cal-

MagNet station about 35 km from the Alum Rock epicenter recorded elevated air conductivity, supporting the regional character of this phenomenon.

It appears that massive air ionization at the rock surface described here provides a valid alternative to the often quoted but never fully tested assumption of increased radon emanation from the ground. If h· charge carriers are stress-activated in the hypocentral volume, they do have the capability to travel long distances through the crust and to reach the Earth's surface. By generating steep electric fields they can ionize the air without a need to close the battery circuit.

However, in addition to the 13 h long pulse of air ionization before the Alum Rock earthquake, the magnetic sensor at the same CalMagNet station also recorded at 50 min long train of intense ULF emission (Bleier et al., 2009). Such ULF signal requires an electric current, e.g. closure of the battery circuit.

The ULF sequence occurred around the midpoint of the 13 h long episode of air ionization. This might have marked the period of most intense ionization. If so, we can imagine a situation in which current closure is achieved by an ion current flowing through the air. Such a scenario for a laboratory experiment is sketched in Fig. 11a. The point to be made here is that, if the airborne ions drift from the positively charged unstressed end to the negatively charged stressed rock, circuit closure is possible.

We can develop this scenario further and apply it to a situation in the field as depicted in Fig. 11b. If there is an area where the stress build-up is so intense that corona discharges occur, for instance above the hypocenter, the surface potential will switch from positive to negative. In this case an electric field gradient develops between the negatively charged center region and the positively charged periphery, where the surface potential continues to be defined by positive holes.

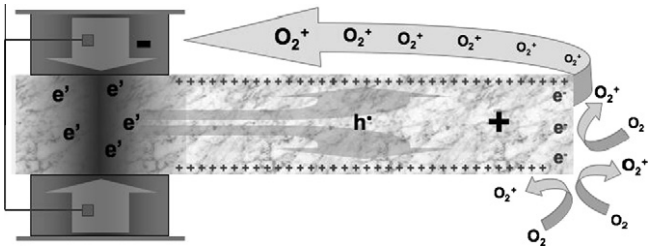

Fig. 11a. Air ionization at the rock surface and closure of the battery circuit due to enhanced air conductivity. O_2 are assumed to be air molecules most likely to be field-ionized.

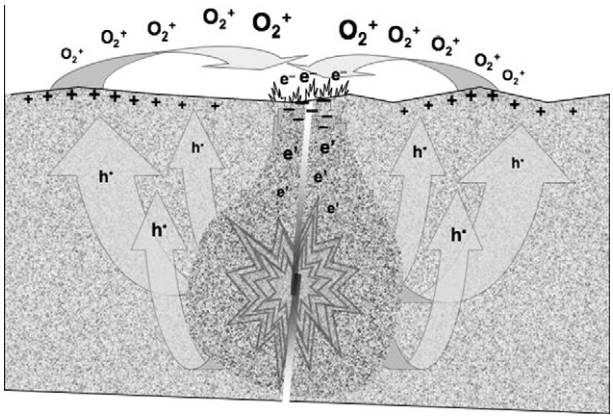

Fig. 11b. Closure of the battery circuit due to enhanced air conductivity above the hypcentral region and reversal of the surface potential. "Flames": corona discharges.

During the laboratory experiments the air ionization rates measured off flat rock surfaces were on the order of 10^9–10^{10} cm^{-2} s^{-1}. Taking the same values and applying them to field situations corresponds to air ion currents on the order of 10–100 A km^{-2}. The currents flowing through the air will provide some level of circuit closure. They appear to be strong enough to account for the intensity of the ULF signals recorded by the CalMagNet sensor prior to the M = 5.4 Alum Rock earthquake (Bleier et al., 2009).

Injection of ions into the air at ground level will have yet other predictable consequences. The airborne ions can act as condensation nuclei for water droplets, leading to fog and haze. The latent heat released during condensation will warm the air and cause it to rise (Dunajecka and Pulinets, 2005). Under the right relative humidity conditions clouds can form.

Cloud formation as a potential indicator of impending seismic activity has been mentioned repeatedly in the literature (Lu, 1988; Ondoh, 2003; Tramutoli, 1998). A few days before the M = 6.7 Bam earthquake of December 26, 2003 in Iran, a distinct cloud formed above the future epicenter, as documented by MeteoSat images (Guo and Wang, 2008). It persisted for about 24 h, drifting ESE for over 2000 km to Gujurat, India. There is no confirmation of increased air ionization from ground stations in the area around Bam around this time.

5.3. Geo-electric anomalies

The electrical resistance of the ground has been monitored for many years, in particular in China, using ground electrode arrays derived from the Schlumberger geoelectric sounding techniques (Patra, 1999). Distinct changes in the resistivity of the soil have been noted, apparently linked to impending earthquake activity. Fig. 12a shows the principle of the measurement where the distance AB is typically 1 km and the distance MN on the order of 200 m (Qian et al., 1983; Zhao and Qian, 1994). The changes in resistivity are usually linked to a presumed build-up of regional stress in the underlying rocks, but there seems to be no detailed understanding of the stress changes. Often a tidal component can be seen in the data, indicating that stresses exerted by the tides have the capability to also affect the electrical conductivity of the top soil.

An example of ground resistivity changes observed in the week before the M = 7.9 Wenchuan earthquake of May 12, 2008 in Sichuan Province, China, is depicted in Fig. 12b (Zhao and Qian, 2009). Small magnitude changes occurred on an almost daily basis, followed by a large drop in ground resistivity a few hours before the earthquake.

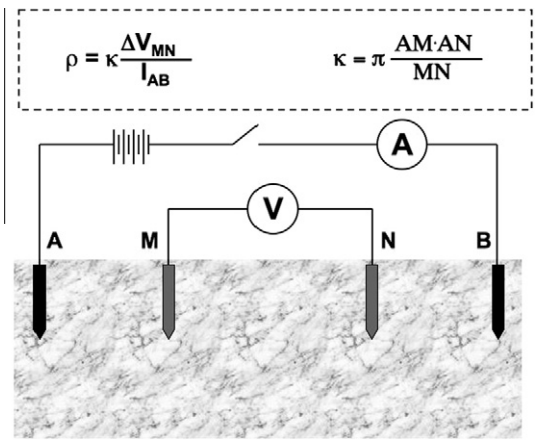

Fig. 12a. Schematic of geoelectric sounding by means of a Schlumberger array.

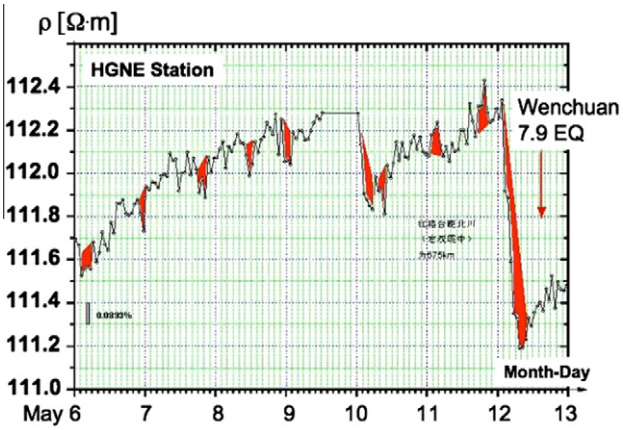

Fig. 12b. Changes in the electric resistivity of the soil prior to the $M = 7.9$ Wenchuan earthquake (after Zhao and Qian (2009)).

In view of stress activation of $h^{\cdot}$ charge carriers at depth and their capability to spread to the Earth surface, the observed changes in soil resistivity are more likely due to waves of $h^{\cdot}$ charge carriers arriving from below rather than to microfracturing of the rocks below the soil caused by stress, which would have to be transmitted over long distances (Qian et al., 1983; Zhao and Qian, 1994).

5.4. Ionospheric perturbations

Numerous examples of ionospheric perturbations have been reported (Chen et al., 2004; Depuev and Zelenova, 1996; Hayakawa et al., 2006; Liu et al., 2004; Liu et al., 2006; Maekawa et al., 2006; Oyama et al., 2008; Pulinets et al., 2005; Singh, 2008; Trigunait et al., 2004; Zakharenkova et al., 2007). They occur in the form of changes in the *F*-region, at altitudes greater than 160 km, and are typically reported as increased Total Electron Content (TEC). They include changes in the subionospheric VLF/LF propagation and shifts in the terminator times (Hayakawa, 2007).

Though pre-earthquake ionospheric perturbations are statistically well documented (Chen et al., 2004) and distinct from the model of the International Reference Ionosphere (Bilitza, 2001), their cause is still not fully understood. Air ionization due to radon release at the ground level has been called into question (Rishbeth, 2006, 2007).

The injection of massive amounts of positive ions at the ground-to-air interface as a result of field ionization of air molecules as described in this report is expected to lead to an upward expansion of highly ionized air and to changes in the vertical electric field between the ground and the lower edge of the ionosphere. The upward drift of airborne ions will form a vertical current, which may reach values on the order of 10–100 A km^{-2}. Such currents, even if they occur only episodically, may play an important role in the global electric circuit (Rycroft et al., 2008). In addition perturbations are expected to occur in the uppermost atmosphere and lower ionosphere (Sorokin et al., 2005; Sorokin et al., 2006). Sky radiation measurements have indicated anomalous values several days before a strong earthquake, both in the red and the green parts of the spectrum. Before and after the $M = 7.4$ Petatlán, Mexico earthquake of March 14, 1979, for instance, large fluctuations in sky luminosity were recorded, at times exceeding the standard value for a transparent atmosphere (Araiza-Quijano and Hernández-del-Valle, 1996). A possible explanation is that massive injection of positive ions at the ground level and their upward expansion led the electrons at the lower edge of the ionosphere to be pulled down and to interact with the uppermost atmosphere, causing the excitation of the 630 nm and 557 nm emission lines of atomic O.

5.5. Light emission and RF noise

If the surface/subsurface electric fields due to an influx of stress-activated positive hole charge carriers become so steep as to trigger corona discharges, visible light will be emitted. Another, still largely speculative possibility is that, at high concentrations, the delocalized wavefunctions of the positive hole charge carriers should begin to overlap, causing a state that may be described as solid state plasma (St-Laurent, 1991). Subvolumes of rocks might enter such a plasma state when the local stresses increase very rapidly. If the solid plasma state becomes unstable and expands, it may lead to sudden outbursts of light at the Earth's surface (St-Laurent, 1991). Together with corona discharges this and other light emission processes falls into the broader group of luminous effects linked to pre-seismic and seismic activity, often referred to as earthquake lights, EQL.

EQLs have been reported since ancient times (Derr, 1973). They have been witnessed at numerous occasions (Galli, 1910; Losseva and Nemchinov, 2005; Mack, 1912; St-Laurent, 2000; Terada, 1931; Tsukuda, 1997), even photographed (Derr, 1986). Many different explanations have been given (Hedervari and Noszticzius, 1985; King, 1983; Ouellet, 1990), often considering piezoelectricity as the physical cause (Finkelstein et al., 1973) or effects of fluids (Lockner et al., 1983; Nur, 1974). How positive hole charge carriers and the delocalization of their associated wavefunctions may cause outbursts of light has been discussed with reference to the $M = 5.9$ Saguenay of November 25, 1988 (St-Laurent et al., 2006), which was remarkable for its 29 km deep hypocenter and large number of EQL reports (St-Laurent, 2000).

EM emissions also occur in other frequencies (Biagi et al., 2001; Dea et al., 1992; Mitzutani and Ishido, 1976; Ohta et al., 2001). A case where radiofrequency (RF) emissions might have played a role has been reported from India: the telemetry of a network of seismometer stations covering an area of 10,000 km^2 around a hydropower dam failed a few days before the on-set of an earthquake swarm about 150 km to the north. The failure progressed from north to south over the course of several days, raising the possibility that the telemetry was overwhelmed by RF noise linked to massive regional corona discharges or other processes at the Earth's surface before the earthquake swarm. Without operator interference the telemetry began to operate again normally after the seismic swarm activity to the north had run its course (Kolvankar, 2001).

Strong and sustained RF emissions have been reported prior to the great Chilean earthquake of May 22, 1960 (Warwick et al., 1982), indicating that the mechanism leading to the RF emission is different from the mechanism proposed above for the much lower frequency range of ULF/ELF emissions. Whereas the ULF/ELF emission can be caused by large $h^{\cdot}$ currents in the crust, possibly at hypocentral depth, RF emissions will require a source at or close to the surface.

5.6. Infrared emission from around epicentral areas

Non-stationary, transient areas of enhanced IR emission have been recognized since the late 1980s and early 1990s in night-time satellite images and linked to impending earthquake activity (Gornyi et al., 1988; Qiang et al., 1991; Qiang et al., 1990; Srivastav et al., 1997). The reported increase in surface temperatures reach 2–4 °C, occasionally higher. This phenomenon has been referred to as "thermal infrared (TIR)" anomalies. Using InSAR data it was shown that the areas, which produce a "thermal anomaly", are

the same that show vertical ground displacements, (Saraf et al., 2008).

The cause for the TIR anomalies has remained enigmatic (Cui et al., 1999; Srivastav et al., 1997; Tronin, 2000a; Tronin, 2002; Tronin et al., 2004). In many cases the reported increase in temperature poorly correlates with meteorological ground data. The rapidity with which the effect appears and disappears rules out that it is due to Joule heat from a deep source flowing to the Earth surface. Other processes that have been invoked include:

(i) rising fluids which would lead to warm gases from the ground (Gornyi et al., 1988);
(ii) rising groundwater levels and changing soil moisture contents (Chadha et al., 2003);
(iii) diffuse CO_2 emanation, causing a "local greenhouse" effect (Quing et al., 1991; Tronin, 1999; Tronin, 2002);
(iv) Near-ground air ionization due to enhanced radon emission leading to condensation of water vapor and, hence, the release of latent heat (Pulinets et al., 2005).

At closer inspection, none of these explanations seems to adequately account for the characteristic features of the reported "thermal anomalies".

The presence of $h^{\cdot}$ charge carriers that form a surface charge layer provide an alternative explanation, which has the advantage of being eminently testable. The basic idea is that, when $h^{\cdot}$ accumulate in the surface/subsurface layer, they can recombine and return to the self-trapped positive hole pair or peroxy state, in which they existed before their stress activation at depth.

It costs energy to break the peroxy bond, probably around 2.4 eV (Freund et al., 1993). When two $h^{\cdot}$ recombine, they can be expected to regain part of this energy, probably around 2.0 eV. The recombination energy will be deposited into the O^-–O^- bond, causing it to be "born" in a vibrationally highly excited state, equivalent to a temperature on the order of 25,000 K.

There are at least two channels for how this highly excited system can get rid of the excess energy and return to the ground state. One possibility is that the excited O^-–O^- bond disproportionates, transferring the energy onto one of its oxygens, which is then released from the surface as an electronically excited neutral O atom. The other possibility is that the excited O^-–O^- bond cascades down its vibrational manifold, emitting IR photons corresponding to the allowed quantum transitions of the O^-–O^- stretching mode. The last transition from the 1st excited state to the ground state, $1 \Rightarrow 0$, lies at 10.7 μm or 930 cm^{-1} (Ricci et al., 2001). Transitions between higher excited states will have energies at slightly longer wavelengths, e.g. lower wavenumbers.

An experiment was set up as shown schematically in the upper right of Fig. 13 (Freund et al., 2007). It used a 60 × 30 × 10 cm^3 slab of anorthosite, a nominally monomineralic feldspar rock, stressed at one end. The IR emission spectrum was recorded off the end of the flat rock, about 50 cm from the stressed volume, using a Bomen MB-100 FT–IR spectroradiometer with a radiometric noise of <10 mK. The IR flux emitted from the rock surface was calculated in brightness temperature units T_B, where the intensity at frequency n is defined as $I_n = B_n(T_B)$ with B_n (J s^{-1} m^{-1} $ster^{-1}$ Hz^{-1}) is given as $B_n \approx 2n^2kT_B/c^2$, with k the Boltzmann constant, T_B the absolute temperature, and c the speed of light. Expressing T_B in terms of wavelength l, we obtain $T_B \approx [l^4/2kc]I_l$.

The upper left of Fig. 13 gives the 294 K emission spectrum for the 8–12.5 μm window as a function of time. The no-load spectrum was recorded during the first 6 min 40 s. Then the load was applied, increasing at a constant rate until failure of the rock after 30 min. The lower right of Fig. 13 gives the difference spectra obtained by subtracting the average of the no-load spectrum from each of the subsequent scans.

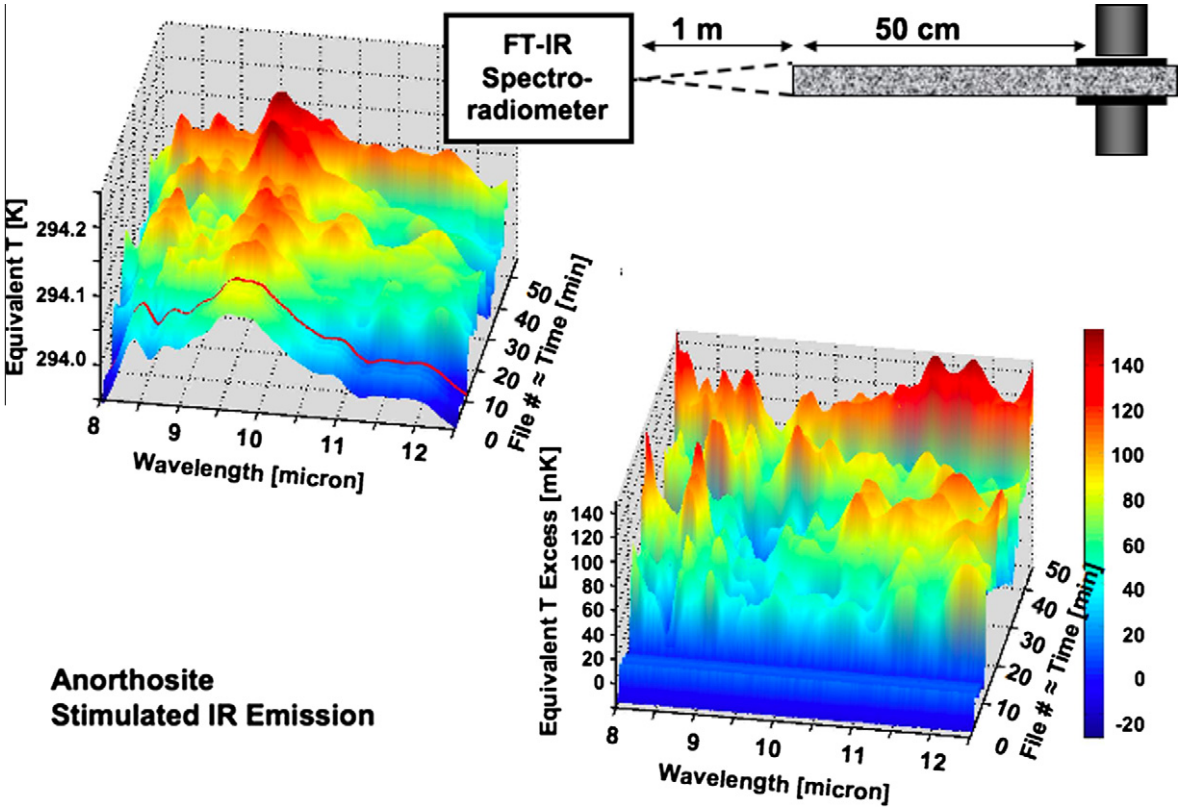

Fig. 13. Upper right: experimental set-up to measure the IR emission from the surface of a rock stressed at the far end. Upper left: IR emission in the 8–12.5 μm range before and during loading up to failure. Lower right: difference spectra showing a series of narrow emission bands.

Most striking are the near-instantaneous and spectroscopically distinct changes in the IR spectrum emitted from the rock surface about 50 cm from where the stress was applied. This IR emission contains narrow bands overlying the broad 294 K thermal emission spectrum, which appear and disappear as the stress build-up progresses. These narrow emission bands indicate that the spectral changes are not those of a gray body emitter and, hence, are not simply due to a increase in the rock surface temperature.

Of particular interest are three bands labeled I, II and III in the lower right side of Fig. 13. They are most clearly seen at the beginning of loading. Band I lies at 10.7 μm (930 cm^{-1}), the energy calculated for the $1 \Rightarrow 0$ transition of the $O^- – O^-$ stretching mode of the $O_3Si–OO–SiO_3$ link (Ricci et al., 2001) and for $O_3Al–OO–SiO_3$ in the feldspar structure (Gianfranco Pacchioni, personal communication, 2005). Bands II and III lie at slightly longer wavelengths (smaller wavenumbers), 11.5 μm (870 cm^{-1}) and 12.35 μm (810 cm^{-1}) respectively. They are consistent with transitions beween the $2 \Rightarrow 1$ and $3 \Rightarrow 2$ vibrational states. Other narrow bands in the 8.0–9.0 μm window are indicative of localized Si–O and Al–O stretching modes excited by energy transfer from the O–O vibrations.

The IR intensity around 9.7 μm (1030 cm^{-1}), the maximum of the 294 K thermal emission, increased only modestly, even though it seems to stand out in the full spectrum in the upper left side of Fig. 13. In fact, the difference spectrum shows a trough at this spectral region, indicating that the sensible temperature of the rock surface barely increased.

Though not simultaneously measured, a positive surface potential certainly built up during stressing due to the influx of $h^\cdot$ to the rock surface. To produce a surface potential around 1 V a charge carrier density on the order of 10^{-5} Coulomb m^{-2} is needed, equivalent to $\approx 10^9$ charges cm^{-2} (Freund, 2002; Freund et al., 2006; Takeuchi and Nagahama, 2002; Takeuchi et al., 2006). To estimate the number of $h^\cdot$ pair recombinations necessary to increase $T_{radiance}$ by 150 mK, we take the energy gained during each recombination event to be 2.0 eV. With this, the energy radiated off the rock surface is equivalent to 10^4–10^5 events, indicating that only a very small fraction, 10^{-4}–10^{-5}, of all $h^\cdot$ arriving at the surface need to participate in recombination events. The pronounced intensity fluctuations suggest that the $h^\cdot$ charge carriers arrive in waves at the rock surface, consistent with the fluctuations seen in the surface potentials and field-ionization experiments.

5.7. Electronically excited oxygen atoms

The other possibility mentioned above for the vibrationally excited $O^- – O^-$ bond to get rid of the excess energy is to disproportionate and to transfer energy onto one of its oxygens, which is then released from the surface at electronically excited O atom. The maximum energy imparted to the O atom would be on the order of 2.0 eV.

Evidence for this decay route might have been accidentally obtained when the light emission was recorded during the failure of rock cylinders using a low-light video camera (Kato et al., 2007). Upon stressing a 5 cm diameter granite cylinder to close to failure a waft of red-glowing air was captured drifting away from the surface. Though the spectrum was not yet recorded, the red color suggests the 630 nm emission line of atomic O, equivalent to 1.97 eV. This observation indicates that the O atoms ejected from the rock surface were excited to the $^3P_2$ level and decayed to the $^1D_2$ level through the emission of 630 nm photons.

If this explanation is correct, it might be possible to detect a weak 630 nm glow in night-time satellite images of pre-earthquake scenes. The red glow would be distinct from the more whitish visible light emission expected if and when corona discharges occur before major earthquakes.

6. Conclusions

The prevailing view in the seismology community is that earthquakes strike without warning and cannot be predicted. The reason for this pessimistic assessment is that the causes for the non-seismic signals, which the Earth reportedly sends out prior to major seismic events, had never been clearly identified. The signals are sometimes strong, more often subtle and fleeting. Their bewildering diversity has been an impediment to finding an answer to the pressing question which process or processes might be able to generate such signals.

Until now each type of reported pre-earthquake signal had solicited an explanation, or several competing explanations, tailored specifically to rationalize this particular effect. This has probably changed now with the discovery that minerals in common crustal rocks contain previously overlooked defects, peroxy links, $O_3Si–OO–SiO_3$, which release electronic charge carriers when subjected to stress. These charge carriers are defect electrons in the oxygen anion sublattice, e.g. electronic states associated with O^- in a matrix of O^{2-}, also known as positive holes. They had first been identified during an electrical conductivity study of nominally high purity MgO single crystals (Kathrein and Freund, 1983) and later more fully characterized by techniques such as magnetic susceptibility and dielectric polarization (Batllo et al., 1991; Freund et al., 1993).

The positive holes have surprising properties, which make them very interesting from the perspective of pre-earthquake signals. They can flow out of the stressed rock volume and spread into the surrounding unstressed or less stressed rocks, traveling fast and far. The countercharges to the positive holes, activated at the same time, are electrons. These electrons cannot leave the stressed subvolume unless special conditions are fulfilled. The situation is akin to a battery, except that the rock battery does not operate on cations and electrons, like an electrochemical battery, but on electronic charge carriers only.

As I have tried to show in this report, most if not all reported pre-earthquake signals seem to be traceable to positive hole charge carriers, their propagation through rocks at depth, their interplay with their counterparts, the electrons, and their multifaceted action at and across the Earth surface. The insight gained by studying rock samples in the laboratory has led to a better understanding of many of the reported pre-earthquake signals and why they are often so transient and fleeting.

In the case of low frequency EM emissions, the reason for their reputed "unreliability" appears to be that sustained positive hole currents in the Earth's crust, capable of emitting a constant stream of EM signals, can only flow when rather stringent conditions are met. The conditions primarily involve closure of the battery circuit. Once positive hole currents begin to flow, they seem to have a natural tendency to fluctuate, both in laboratory experiments and in the field.

These fluctuations may be due to coupling to other processes yet to be fully understood. We may also look at positive hole currents from a different angle, emphasizing the fact that, when $h^\cdot$ charge carriers flow out of a stressed rock volume in large numbers and propagate through the Earth crust, they will probably begin as a more or less uniform current filling a wide cross section. Any current generates its own magnetic field, however, which interacts with the Earth's magnetic field. Even if an $h^\cdot$ current in the crust starts out homogeneously, as a uniform volume current, its interaction with the Earth magnetic field will cause it to break up into current packets, even if the crust were homogeneous with respect to its resistance and current carrying capacity. These current packets will manifest themselves as intensity fluctuations of the EM emissions.

Fundamentally the conditions in the Earth's crust are similar to those which control currents from a conventional battery: whether continuous or fluctuating, currents can flow only when the battery circuit is closed. While it is easy to close the battery circuit in laboratory experiments by running a wire from the stressed to the unstressed rock subvolumes, closure of the battery circuit in the Earth's crust is difficult to achieve. Three scenarios have so far been identified as mentioned in Section 4.1, each expected to give rise to EM signals under a different set of restrictions. Understanding these restrictions may help understand why is has often been difficult to capture pre-earthquake EM signals and why they even seem to be absent before certain major seismic events.

The good news is that not all processes which can produce pre-earthquake signals require closure of the battery circuit. Foremost among them are processes that take place at the ground-to-air interface during the build-up of surface/subsurface charge layers, when $h^{\cdot}$ charge carriers from below arrive at the Earth's surface. This $h^{\cdot}$ flow is independent of battery circuit closure and should thus provide more sturdy pre-earthquake signals.

One such process at the ground-to-air interface leads to ionization of air. If ionization occurs without corona discharges, it will produce only positive airborne ions. If corona discharges build-up, the ionization will produce mixtures of both positive and negative ions, in addition to free electrons. The rate of air ionization demonstrated in laboratory experiments is far higher than what can be reasonably expected for radon emanatation from the ground. Understanding how this $h^{\cdot}$–driven air ionization works and under which conditions it is most likely to occur in the field alleviates the need to assign to radioactive radon a role which this rare gas cannot play.

Another important process at the ground-to-air interface pertains to the pre-earthquake "thermal anomalies" seen in nighttime infrared satellite images. The question as to why and how this kind of infrared emission occurs has been discussed widely, and often controversially, over the course of the past two decades. Understanding the physics of $h^{\cdot}$ charge carriers and their accumulation in a thin surface/subsurface layer provides an answer that is fundamentally different from all other explanations offered so far. As outlined in Section 5.6, the excess IR radiation may be due to the pairwise recombination of $h^{\cdot}$ charge carriers, which allows them to return to the peroxy state. The energy released during this reaction causes the two oxygens to become vibrationally highly excited (Section 5.7). They can de-excite through a series of quantum mechanically allowed transitions, emitting IR photons of specific wavelengths. This non-thermal IR emission fortuitously lies in the same spectral region as the IR emission from a gray body at temperatures around 300 K. However it is spectroscopically distinct as demonstrated in laboratory experiments.

Our new and fundamentally different approach provides the possibility to address the excess IR radiation coming from the Earth surface around future epicenters. It also provides the basis for a prediction that, in addition to the non-thermal IR emission, a parallel process should produce electronically excited O atoms, which will give rise to a distinctive red glow at 630 nm.

The study of $h^{\cdot}$ charge carriers allows us to look at the diversity of reported pre-earthquake signals from the unifying perspective of solid state physics. It allows us to go beyond the patchwork of separate explanations aimed at different types of pre-earthquake signals, which has been a source of disagreement and controversy in the past.

Acknowledgments

This paper reviews work that spans several decades. During the past few years work was carried out in collaboration with Akihiro Takeuchi (supported by a grant from JSPS, Japan Society for the Promotion of Science), Bobby Lau (supported by a grant from NIMA/NGA, National Imaging and Mapping Agency/National Geospatial Agency), Melike Balk (supported by a travel grant from NOW, Netherlands Organization for Scientific Research), Ipek Kulahci (supported by a grant from NASA Exobiology), Gary Cyr and Robert Dahlgren (supported by a grant from NASA's Earth Surface and Interior Program), Milton Bose (supported by a grant from NSF-REU Research Experience for Undergraduates to San Jose State University Physics Department). This work also received partial funding from the NASA Ames Director's Discretionary Fund and the NASA Astrobiology Institute (NAI) Cooperative Agreement NNA04CC05A to the SETI Institute. FF acknowledges the receipt of a Fellowship from the NASA Goddard Earth Science and Technology (GEST) program during part of the time and valuable contributions from Patrick Taylor, Dimitar Ouzounov and Hollis H. Jones, all at NASA Goddard Space Flight Center. The work benefited from discussions with Vern Vanderbilt, NASA Ames Research Center, and from contributions by students: James King and Jeremy Tregloan-Reed (University of Lancaster, UK) and Julia Ling (Princeton University). Access to equipment used in this study was provided by Akthem Al-Manaseer, Department of Civil Engineering, San Jose State University, San Jose, CA, by Charles Schwartz, Department of Civil Engineering, University of Maryland, College Park, MD, and by Jerry Wang, Lynn Hofland, and Frank Pichay, Engineering Evaluation Laboratory at the NASA Ames Research Center.

References

Anastasiadis, C. et al., 2007. Comments on the phenomena underlying pressure stimulated currents in dielectric rock materials. J. Mater. Sci. 42 (8), 2538–2542.
Araiza-Quijano, M.R., Hernández-del-Valle, G., 1996. Some observations of atmospheric luminosity as a possible earthquake precursor. Geofis. Internacional 35, 403–408.
Aydin, A. et al., 2009. Observation of pressure stimulated voltages in rocks using an electric potential sensor. Appl. Phys. Lett. 95, 124102.
Balbachan, M.Y., Parkhomenko, E.I., 1983. Electret effect during rupture of rocks. Isv., Phys. Solid Earth 19, 661–665.
Balbachan, M.Y., Tomashevskaya, I.S., 1987. Change in rock strength as a result of mechanical induction of charges. Dokl. Akad. Nauk, SSR 296, 1085–1089.
Batllo, F. et al., 1991. Positive hole centers in magnesium oxide – correlation between magnetic susceptibility, dielectric anomalies and electric conductivity. J. Appl. Phys. 69, 6031–6033.
Bernabé, Y., 1998. Streaming potential in heterogenous networks. J. Geophys. Res. 103 (B9), 20827–20841.
Biagi, P.F. et al., 2001. Possible earthquake precursors revealed by LF radio signals. Nat. Hazards Earth Syst. Sci. 1, 99–104.
Bilitza, D., 2001. International reference ionosphere 2000. Radio Sci. 36 (2), 261–275.
Bishop, J.R., 1981. Piezoelectric effects in quartz-rich rocks. Tectonophysics 77, 297–321.
Bleier, T. et al., 2009. Investigation of ULF magnetic pulsations, air conductivity changes, and infra red signatures associated with the 30 October 2007 Alum Rock M5.4 earthquake. Nat. Hazards Earth Syst. Sci. 9, 585–603.
Brace, W.F., 1975. Dilatancy-related electrical resistivity change in rocks. Pure Appl. Geophys. 113, 207–217.
Brace, W.F. et al., 1966. Dilatancy in the fracture of crystalline rocks. J. Geophys. Res. 71, 3939–3953.
Brady, B.T., 1992. Electrodynamics of Rock Fracture – Implications for Models of Rock Fracture, Paper Presented at Low Frequency Electrical Precursors: Fact of Fiction? NSF National Earthquake Hazard Reduction Program, Lake Arrowhead, CA, USA June 14–17, 1992.
Brady, B.T., Rowell, G.A., 1986. Laboratory investigation of the electrodynamics of rock fracture. Nature 321, 488–492.
Cervone, G. et al., 2006. Surface latent heat flux and nighttime LF anomalies prior to the Mw = 8.3 Tokachi-Oki Earthquake. Nat. Hazards Earth Syst. Sci. 6 (1), 109–114.
Chadha, R.K. et al., 2003. Search for earthquake precursors in well water levels in a localized seismically active area of Reservoir Triggered Earthquakes in India. Geophy. Res. Lett. 30 (7), 69–71.
Chen, Y.L. et al., 1999. A Statistical Study of Ionospheric Precursors of Strong Earthquakes in the Taiwan Area, Paper Presented at 24th General Ass. URSI, URSI.
Chen, Y.I. et al., 2004. Statistical test for pre-earthquake ionospheric anomaly. Terr. Atmos. Ocean. Sci. 15, 385–396.
Chyi, L.L. et al., 2002. Automated radon monitoring of seismicity in a fault zone. Geofis. Internacional 41 (4), 507–511.

Console, R. et al., 2002. Probabilistic approach to earthquake prediction. Ann. Geophys. 45 (6), 723–731.

Cristescu, N., 1982. Rock dilatancy in uniaxial tests. Rock Mech. Rock Eng. 15 (3), 133–144.

Cui, C. et al., 1999. Monitoring the Thermal IR Anomaly of Zhangbei Earthquake Precursor by Satellite Remote Sensing Technique, Paper Presented at ACRS.

Cullity, B.D., 1971. Fundamentals of magnetostriction. J. Metals 1, 35–41.

Darnet, M., Marquis, G., 2003. Modelling streaming potential (SP) signals induced by water movement in the vadose zone. J. Hydrol. 285 (1–4), 114–124.

Dea, J.Y. et al., 1992. Sensing of seismo-electromagnetic earthquake precursor radiation signatures along Southern California fault zones: evidence of long distance precursor ULF signals observed before a moderate Southern California earthquake episode. In: AGARD, Remote Sensing of the Propagation Environment, vol. 8, pp. 13–46.

Depuev, V., Zelenova, T., 1996. Electron density profile changes in a pre-earthquake period. Adv. Space Res. 18 (6), 115–118.

Derr, J.S., 1973. Earthquake lights: a review of observations and present theories. Bull. Seismol. Soc. Am. 63, 2177–2187.

Derr, J.S., 1986. Luminous phenomena and their relationship to rock fracture. Nature 321, 470–471.

Dobrovolsky, I.P. et al., 1979. Estimation of the size of earthquake preparation zones. Pure Appl. Geophys. 117, 1025–1044.

Dunajecka, M.A., Pulinets, S.A., 2005. Atmospheric and thermal anomalies observed around the time of strong earthquakes in México. Atmósfera 18 (4), 236–247.

Enomoto, Y., Hashimoto, H., 1990. Emission of charged particles from indentation fracture of rocks. Nature 346, 641–643.

Enomoto, Y. et al., 1993. Exoelectron emission: possible relation to seismic geo-electromagnetic activities as a microscopic aspect in geotribology. Wear 168, 135–142.

Finkelstein, D. et al., 1973. The piezoelectric theory of earthquake lightning. J. Geophys. Res. 78, 992–993.

Freund, F., 1985. Conversion of dissolved "water" into molecular hydrogen and peroxy linkages. J. Non-Cryst. Solids 71, 195–202.

Freund, F., 2002. Charge generation and propagation in rocks. J. Geodyn. 33 (4–5), 545–572.

Freund, F.T., 2007a. Pre-earthquake signals – part II: flow of battery currents in the crust. Nat. Hazards Earth Syst. Sci. 7, 1–6.

Freund, F.T., 2007b. Pre-earthquake signals – part I: deviatoric stresses turn rocks into a source of electric currents. Nat. Hazards Earth Syst. Sci. 7, 1–7.

Freund, F.T., 2009. Stress-activated positive hole charge carriers in rocks and the generation of pre-earthquake signals. In: Hayakawa, M. (Ed.), Electromagnetic Phenomena Associated with Earthquakes. Research Signpost, New Dehli, pp. 41–96.

Freund, F. et al., 1993. Critical review of electrical conductivity measurements and charge distribution analysis of magnesium oxide. J. Geophys. Res. 98 (B12), 22209–22229.

Freund, F.T. et al., 2006. Electric currents streaming out of stressed igneous rocks – a step towards understanding pre-earthquake low frequency EM emissions. Phys. Chem. Earth 31 (4–9), 389–396.

Freund, F.T. et al., 2007. Stimulated thermal IR emission from rocks: assessing a stress indicator. eEarth 2, 1–10.

Freund, F.T. et al., 2009. Air ionization at rock surface and pre-earthquake signals. J. Atmos. Sol. Terr. Phys. 71, 1824–1834.

Galdin, N.V. et al., 1986. Thermal conductivities of dry and water-saturated low-porosity crystalline rocks of the Archean Kola series. Int. Geol. Rev. 28 (7), 858–865.

Galli, I., 1910. Raccolta e classifzione di fenomeni luminosi osservati nei terremoti. Bolletino della Societa Sismological Italiana 14, 221–448.

Geller, R.J. et al., 1997. Earthquakes cannot be predicted. Science 275, 1616–1617.

Gornyi, V.I. et al., 1988. The Earth's outgoing IR radiation as an indicator of seismic activity. Proc. Acad. Sci. USSR 301 (1), 67–69.

Gringel, W. et al., 1986. Electrical structure from 0 to 30 kilometers. In: The Earth's Electrical Environment. National Academic Press, Washington, DC, pp. 166–182.

Griscom, D.L., 1990. Electron spin resonance. Glass Sci. Technol. 4B, 151–251.

Grunewald, E.D., Stein, R.S., 2006. A new 1649–1884 catalog of destructive earthquakes near Tokyo and implications for the long-term seismic process. J. Geophys. Res. 111 (B12), B12306.

Guo, G., Wang, B., 2008. Cloud anomaly before Iran earthquake. Int. J. Remote Sens. 29 (7), 1921–1928.

Hadjicontis, V., Mavromatou, C., 1994. Transient electric signals prior to rock failure under uniaxial stress. Geophys. Res. Lett. 21, 1687–1690.

Hadjicontis, V., Mavromatou, C., 1995. Electric signals recorded during uniaxial compression of rock samples: their possible correlation with preseismic electric signals. Acta Geophys. Polonica 43 (1), 49–61.

Hadjicontis, V. et al., 2005. Memory effects in EM emission during uniaxial deformation of dielectric crystalline materials. IEEE Geosci. Remote Sens. Lett. 2 (2), 118–120.

Hadjicontis, V. et al., 2007. Mechanism of electromagnetic emission in plastically deformed ionic crystals. Phys. Rev. B 76, 024106.

Hadley, K.J., 1975. Azimuthal variation of dilatancy. J. Geophys. Res. 80, 4845–4850.

Hattori, K. et al., 2008. Variation of Radioactive Atmospheric Ion Concentration Associated with Large Earthquakes, Paper Presented at AGU Fall Meeting, San Francisco, CA.

Hawking, S., 2003. On the Shoulders of Giants. Running Press.

Hayakawa, M., 2007. VLF/LF radio sounding of ionospheric perturbations associated with earthquakes. Sensors 7, 1141–1158.

Hayakawa, M., Molchanov, O.A., 1998. On the generation mechanism of ULF seismogenic electromagnetic emissions. Phys. Earth Planet. Int. 105 (3–4), 201–210.

Hayakawa, M. et al., 2005. Subionospheric LF monitoring of ionospheric perturbations prior to the Tokachi-oki earthquake and a possible mechanism of lithosphere–ionosphere coupling. Adv. Polar Upper Atmos. Res. 18, 42–54.

Hayakawa, M. et al., 2006. Recent progress in seismo electromagnetics and related phenomena. Phys. Chem. Earth 31 (4–9), 129–131.

Hedervari, P., Noszticzius, Z., 1985. Recent results concerning earthquake lights. Ann. Geophys. 3 (6), 705–708.

Hollerman, W.A. et al., (2006). Electric Currents in Granite and Gabbro Generated by Impacts up to 1 km/s, Paper Presented at AGU Fall Meeting, AGU, San Francisco.

Hoppel, W.A. et al., 1986. Atmospheric electricity in the planetary boundary layer. In: The Earth's Electrical Environment. National Academic Press, Washington, DC, pp. 149–165.

Huang, Q., 2002. One possible generation mechanism of co-seismic electric signals. Proc. Jpn. Acad. Ser. B: Phys. Biol. Sci. 78 (7), 173–178.

Ikeya, M. et al., 1996. Ground electric field effects on rats and sparrows: seismic anomalous animal behaviors (SAABs). Jpn. J. Appl. Phys. 35, 4587–4594.

İnan, S.T. et al., 2008. Geochemical monitoring in the Marmara region (NW Turkey): a search for precursors of seismic activity. J. Geophys. Res. 113. B03401. doi:03410.01029/02007JB005206.

Inubushi, H., 2005. Apparatus and Method for Analyzing Correlation Between Geophysical Data and Seismic Data, Geophysical Data Monitoring Apparatus and Method, and Earthquake Monitoring Method, United States Patent 6859416.

Johnston, M.J.S., 1997. Review of electric and magnetic fields accompanying seismic and volcanic activity. Surv. Geophys. 18, 441–475.

Jouniaux, L. et al., 2006. Electrical conductivity evolution of non-saturated carbonate rocks during deformation up to failure. Geophys. J. Int. 167 (2), 1017–1026.

Kathrein, H., Freund, F., 1983. Electrical conductivity of magnesium oxide single crystals below 1200 K. J. Phys. Chem. Solids 44, 177–186.

Kato, M. et al., 2007. Experimental studies on luminescence of visible lights associated with rock fracture. In: IUGG 2007, Perugia, Italy, p. 7501.

King, C.-Y., 1980. Episodic radon changes in subsurface soil gas along active faults and possible relation to earthquakes. J. Geophys. Res. 85 (B6), 3065–3078.

King, C.-Y., 1983. Electromagnetic emission before earthquakes. Nature 301, 377.

King, B.V., Freund, F., 1984. Surface charges and subsurface space charge distribution in magnesium oxide containing dissolved traces of water. Phys. Rev. B29, 5814–5824.

Kirschvink, J.L., 2000. Earthquake prediction by animals: evolution and sensory perception. Bull. Seismol. Soc. Am. 90 (2), 312–323.

Kolvankar, V.G., 2001. Report BARC-2001/E/006: Earthquake Sequence of 1991 from Valsad Region, Guajrat, BARC-2001/E/006, Bhabha Atomic Research Centre, Seismology Div., Mumbai, India, 68 pp.

Kyriazis, P. et al., 2009. Modelling of electric signals stimulated by bending of rock beams. Int. J. Microstruct. Mater. Prop. 4 (1), 5–18.

Lebedev, A.V. et al., 2003. Resonant acoustic spectroscopy of microfracture in a Westerly granite sample. J. Geophys. Res. 108 (B10), 2500.

Lei, X. et al., 2000. Quasi-static fault growth and cracking in homogeneous brittle rock under triaxial compression using acoustic emission monitoring. J. Geophys. Res. 105 (B3), 6127–6140.

Liperovsky, V.A. et al., 2000. Modification of sporadic E-layers caused by seismic activity. Surv. Geophys. 21 (5–6), 449–486.

Liu, J.Y. et al., 2004. Pre-earthquake ionospheric anomalies registered by continuous GPS TEC measurements. Ann. Geophys. 22, 1585–1593.

Liu, J.Y. et al., 2006. A statistical investigation of preearthquake ionospheric anomaly. J. Geophys. Res. 111. A05304. doi:05310.01029/02005JA011333.

Lockner, D.A. et al., 1983. A mechanism for the generation of earthquake lights. Nature 302, 28–33.

Logan, J.M., 1977. Animal behavior and earthquake prediction. Nature 265, 404–405.

Losseva, T.V., Nemchinov, I.V., 2005. Earthquake lights and rupture processes. Nat. Hazards Earth Syst. Sci. 5, 649–656.

Lu, D., 1988. Impending Earthquake Prediction. Jinangsu Science and Publishing House, Nanjing, China. 46 Plus Supplement pp..

Mack, K., 1912. Das süddeutsche Erdbeben vom 16. November 1911, Abschnitt VII: Lichterscheinungen. In: Würtembergische Jahrbücher für Statistik and Landeskunde, Stuttgart, p. 131.

Maekawa, S. et al., 2006. A statistical study on the effect of earthquakes on the ionosphere, based on the subionospheric LF propagation data in Japan. Ann. Geophys. 24, 2219–2225.

Main, I.G., 1996. Statistical physics, seismogenesis, and seismic hazard. Rev. Geophys. 34 (4), 433–462.

Manna, S.S., Chakrabarti, B.K., 1987. Dielectric breakdown in the presence of random conductors. Phys. Rev. B Solid State 36 (7), 4078–4081.

Merzer, M., Klemperer, S.L., 1997. Modeling low-frequency magnetic-field precursors to the Loma Prieta earthquake with a precursory increase in fault-zone conductivity. Pure Appl. Geophys. 150, 217–248.

Milne, J., Lee, A.W., 1939. Earthquakes and Other Earth Movements, seventh ed. Kegan Paul, Trench, Trubner & Co., London. 242 pp..

Mitzutani, H., Ishido, T., 1976. A new interpretation of magnetic field variation associated with the Matsushiro earthquakes. J. Geomagn. Geoelectr. 28, 179–188.

Morrison, F.D. et al., 1989. Streaming potentials of Westerly granite with applications. J. Geophys. Res. 94, 12449–12461.

Mulargia, F., Geller, R. (Eds.), 2003. Earthquake Science and Seismic Risk Reduction. Springer, Berlin.

Nagarajaa, K. et al., 2003. Radon and its short-lived progeny: variations near the ground. Radiat. Meas. 36 (1–6), 413–417.

Nedderman, R.M., 1992. Statics and Kinematics of Granular Materials. Cambridge University Press.

Nur, A., 1974. Matsushiro, Japan, earthquake swarm: confirmation of the dilatancy-fluid diffusion model. Geology 2, 217–221.

Ogawa, T., Utada, H., 2000a. Electromagnetic signals related to incidence of a teleseismic body wave into a subsurface piezoelectric body. Earth Planets Space 52, 253–256.

Ogawa, T., Utada, H., 2000b. Coseismic piezoelectric effects due to a dislocation. 1. An analytical far and early-time solution in a homogeneous whole space. Phys. Earth Planet. Int. 121, 273–288.

Ohta, K. et al., 2001. ULF/ELF emissions observed in Japan, possibly associated with the Chi–Chi earthquake in Taiwan. Nat. Hazards Earth Syst. Sci. 1, 37–42.

Omori, Y. et al., 2009. Preseismic alteration of atmospheric electric conditions due to anomalous radon emanation. Phys. Chem. Earth 34, 435–440.

Ondoh, T., 2003. Anomalous sporadic-E layers observed before M 7.2 Hyogo-ken Nanbu earthquake; terrestrial gas emanation model. Adv. Polar Upper Atmos. Res. 17, 96–108.

Oster, L. et al., 1999. Classification of exoelectron emission mechanisms. Phys. Status Solidi 174 (2), 431–439.

Ouellet, M., 1990. Earthquake light and seismicity. Nature 348, 492.

Ouzounov, D., Freund, F.T., 2004. Mid-infrared emission prior to strong earthquakes analyzed by remote sensing data. Adv. Space Res. 33, 268–273.

Ouzounov, D. et al., 2006. Satellite thermal IR phenomena associated with some of the major earthquakes in 1999–2003. Phys. Chem. Earth 31 (4–9), 154–163.

Ouzounov, D. et al., 2007. Outgoing long wave radiation variability from IR satellite data prior to major earthquakes. Tectonophysics 431 (1–4), 211–220.

Oyama, K.I. et al., 2008. Reduction of electron temperature in low-latitude ionosphere at 600 km before and after large earthquakes. J. Geophys. Res. 113. A11317.

Papathanassiou, A.N., 2000. Polarization and depolarization currents resulting from the temperature or pressure induced volume changes in polarized dielectrics. J. Phys.: Condens. Matter 12, 9985–9992.

Parkhomenko, E.I., Bondarenko, A.T., 1986. Electrical conductivity of rocks at high pressures and temperatures. In: Elektroprovodnost Gornykh Porod Privysokikh Davleniyakh i Temperaturakh, Moscow 1972, NASA, 212 pp.

Patra, H.P., 1999. Schumberger Geolectric Sounding in Ground Water. A.A. Balkema, Rotterdam, NL.

Pulinets, S., 2007. Natural radioactivity, earthquakes, and the ionosphere. EOS 88 (20). doi:10.1029/2007EO200001.

Pulinets, S., 2009. Physical mechanism of the vertical electric field generation over active tectonic faults. Adv. Space Res. 44, 767–773. doi:10.1016/j.asr.2009.04.038.

Pulinets, S., Boyarchuk, K., 2004. Ionospheric Precursors of Earthquakes. Springer, Heidelberg.

Pulinets, S.A., Dunajeck, M.A., 2006. Specific variations of air temperature and relative humidity around the time of Michoacan earthquake M8.1 September 19, 1985 as a possible indicator of interaction between tectonic plates. Tectonophysics 431 (1–4), 221–230.

Pulinets, S.A. et al., 1997. Radon and metallic aerosols emanation before strong earthquakes and their role in atmosphere and ionosphere modification. Adv. Space Res. 20 (11), 2173–2176.

Pulinets, S.A. et al., 2005. Total electron content variations in the ionosphere before the Colima, Mexico, earthquake of 21 January 2003. Geofis. Internacional 44 (4), 369–377.

Pulinets, S.A. et al., 2006. Thermal, atmospheric and ionospheric anomalies around the time of the Colima M7.8 earthquake of 21 January 2003. Ann. Geophys. 24, 835–849.

Qian, F. et al., 1983. Geoelectric resistivity anomalies before earthquakes. Sci. Sin. B 26, 326–336.

Qiang, Z.J. et al., 1990. Abnormal infrared thermal of satellite-forewarning of earthquakes. Chin. Sci. Bull. 35 (17), 1324–1327.

Qiang, Z.-J. et al., 1991. Thermal infrared anomaly–precursor of impending earthquakes. Chin. Sci. Bull. 36 (4), 319–323.

Qiang, Z. et al., 1999. Satellite thermal infrared brightness temperature anomaly image: short-term and impending earthquake precursors. Sci. China, Ser. D: Earth Sci. 42 (3), 313–324.

Quing, Z. et al., 1991. Thermal infrared anomaly–precursor of impending earthquakes. Chin. Sci. Bull. 36 (4), 319–323.

Ricci, D. et al., 2001. Modeling disorder in amorphous silica with embedded clusters: the peroxy bridge defect center. Phys. Rev. B 64 (22). 224104-1–224104-8.

Rishbeth, H., 2006. F-region links with the lower atmosphere? J. Atmos. Sol. Terr. Phys. 68 (3–5), 469–478.

Rishbeth, H., 2007. Do earthquake precursors really exist? EOS 88 (29). doi:10.1029/2007EO290008.

Rycroft, M.J. et al., 2008. An overview of Earth's global electric circuit and atmospheric conductivity. Space Sci. Rev. 137 (1-4), 83–105.

Saraf, A.K. et al., 2008. Satellite detection of earthquake thermal infrared precursors in Iran. Nat. Hazards 47, 119–135.

Sasai, Y., 1979. The piezomagnetic field associated with the Mogi model. Bull. Earthquake Res. Inst. Univ. Tokyo 54, 1–29.

Sasai, Y., 1991. Tectonomagnetic modeling on the basis of the linear piezomagnetic effect. Bull. Earthq. Res. Inst., Univ. Tokyo 66, 585–722.

Sasai, Y., 2001. Tectonomagnetic modeling based on the piezomagnetism: a review. Ann. Geofis..

Savage, J.C. et al., 1996. Failure in laboratory fault models in triaxial tests. J. Geophys. Res. 101 (B10), 22215–22224.

Schall, R.B., 1988. An evaluation of the animal-behavior theory for earthquake prediction. Calif. Geol. 41 (2), 41–45.

Scholz, C.H., 1978. Velocity anomalies in dilatant rock. Science 201 (4354), 441–442.

Scholz, C.H., 2002. The Mechanism of Earthquakes and Faulting, second ed. Cambrdge University Press, Cambridge, UK. 470 pp..

Shluger, A.L. et al., 1992. Theoretical simulation of localized holes in MgO. J. Phys.: Condens. Matter 4 (26), 5711–5722.

Singh, B., 2008. Electromagnetic Phenomenon Related to Earthquakes and Volcanoes. Narosa Publ. House, New Delhi. 264 pp..

Smith, B.J. et al., 2007. Iowa radon leukaemia study: a hierarchical population risk model for spatially correlated exposure measured with error. Stat. Med. 26, 4619–4642.

Sober, E., 1994. Let's Razor Occam's Razor. In: Knowles, D. (Ed.), Explanation and Its Limits. Cambridge University Press, pp. 73–93.

Sornette, A., Sornette, D., 1990. Earthquake rupture as a critical point: consequences for telluric precursors. Tectonophysics 179, 327–334.

Sorokin, V.M. et al., 2005. Possible DC electric field in the ionosphere related to seismicity. Adv. Space Res. 37 (4), 666–670.

Sorokin, V.M. et al., 2006. Formation mechanism of the lower-ionospheric disturbances by the atmosphere electric current over a seismic region. J. Atmos. Sol. Terr. Phys. 68 (11), 1260–1268.

Srivastav, S.K. et al., 1997. Satellite data reveals pre-earthquake thermal anomalies in Killari area, Maharashtra. Curr. Sci. 72 (11), 880–884.

Stacey, F.D., Johnston, M.J.S., 1972. Theory of piezomagnetic effect in titanomagnetite-bearing rocks. Pure Appl. Geophys. 97, 146–155.

Stewart, T.R., 2000. Uncertainty, judgment, and error in prediction. In: Sarewitz, D. et al. (Eds.), Prediction: Science, Decision Making, and the Future of Nature. Island Press, Washington, DC, pp. 41–57.

St-Laurent, F., 1991. Corona effect and electro-atmospheric discharges: possible luminous effect following earthquakes? J. Meteorol. (UK) 16, 238–241.

St-Laurent, F., 2000. The Saguenay, Québec, earthquake lights of November 1988–January 1989. Seismolog. Res. Lett. 71 (2), 160–174.

St-Laurent, F. et al., 2006. Earthquake lights and the stress-activation of positive hole charge carriers in rocks. Phys. Chem. Earth 31 (4–9), 305–312.

Suess, M.J., 2004. Radon indoors: a risk-based approach to health protection criteria. Indoor Air 4 (3), 197–201.

Takahashi, I. et al., 2007. Anomalous geoelectrical and geomagnetic signals observed at Southern Boso Peninsula, Japan. Ann. Geophys. 50 (1), 123–135.

Takeuchi, A., Nagahama, H., 2002. Interpretation of charging on fracture or frictional slip surface of rocks. Phys. Earth Planet. Int. 130, 285–291.

Takeuchi, A. et al., 2006. Current and surface potential induced by stress-activated positive holes in igneous rocks. Phys. Chem. Earth 31 (4–9), 240–247.

Teisseyre, R., 1983. Premonitory mechanism and resistivity variations related to earthquake. Pure Appl. Geophys. 121 (2), 297–315.

Terada, T., 1931. On luminous phenomena accompanying earthquakes. Bull. Earthquake Res. Inst. Tokyo Univ. 9, 225–255.

Tramutoli, V., 1998. Robust AVHRR Techniques (RAT) for Environmental Monitoring: Theory and Applications, Paper Presented at EUROPTO Conference on Remote Sensinci for Geolociy, Land Management, and Cultural Heritage Ill, SPIE, Barcelona, Spain.

Tramutoli, V. et al., 2005. Assessing the potential of thermal infrared satellite surveys for monitoring seismically active areas: the case of Kocaeli (Izmit) earthquake, August 17, 1999. Remote Sens. Environ. 96, 409–426.

Trigunait, A. et al., 2004. Variations of the ionospheric electron density during the Bhuj seismic event. Ann. Geophys. 22 (12), 4123–4131.

Tronin, A.A. (Ed.), 1999. Satellite Thermal Survey Application for Earthquake Prediction. Terra Sci. Publ., Tokyo, Japan, pp. 717–746.

Tronin, A.A., 2000a. Thermal Satellite Data for Earthquake Research, Paper Presented at IGARSS 2000; IEEE 2000 International Geoscience and Remote Sensing Symposium. Taking the Pulse of the Planet: the Role of Remote Sensing in Managing the Environment, IEEE, Honolulu, HI.

Tronin, A.A., 2000b. Thermal IR satellite sensor data application for earthquake research in China. Int. J. Remote Sens. 21 (16), 3169–3177.

Tronin, A.A., 2002. Atmosphere–lithosphere coupling: thermal anomalies on the Earth surface in seismic process. In: Hayakawa, M., Molchanov, O.A. (Eds.), Seismo-Electromagnetics: Lithosphere–Atmosphere–Ionosphere Coupling. Terra Scientific Publ., Tokyo, pp. 173–176.

Tronin, A.A. et al., 2004. Thermal anomalies and well observations in Kamchatka. Int. J. Remote Sens. 25 (13), 2649–2655.

Tsukuda, T., 1997. Sizes and some features of luminous sources associated with the 1995 Hyogo-ken Nanbu earthquake. J. Phys. Earth 45, 73–82.

Tsvetkova, T. et al., 2001. Research on variation of radon and gamma-background as a prediction of earthquakes in the Caucasus. Radiat. Meas. 33, 1–5.

Tuck, B.T. et al., 1977. A search for the piezoelectric effect in quartz-bearing rock. Tectonophysics 39, 7–11.

Turcotte, D.L., 1991. Earthquake prediction. Ann. Rev. Earth Planet. Sci. 19, 263–281.

Tzanis, A. et al., 2000. Identification and discrimination of transient electrical earthquake precursors: fact, fiction and some possibilities. Phys. Earth Planet. Int. 121 (3–4), 223–248.
Uyeda, S. et al., 2009a. Analysis of electrical activity and seismicity in the natural time domain for the volcanic-seismic swarm activity in 2000 in the Izu Island region, Japan. J. Geophys. Res. 114, B02310.
Uyeda, S. et al., 2009b. Short-term earthquake prediction: current status of seismo-electromagnetics. Tectonophysics 470, 205–213.
Vallianatos, F., Triantis, D., 2008. Scaling in pressure stimulated currents related with rock fracture. Phys. A: Stat. Mech. Appl. 387 (19-20), 4940–4946.
Varotsos, P.A., 2005. The Physics of Seismic Electric Signals. Terra Scientific Publishing Co., Tokyo. 388 pp.
Varotsos, P., Alexopoulos, K., 1987. Physical properties of the variations of the electric field of the earth preceding earthquakes, III. Tectonophysics 136, 335–339.
Varotsos, P. et al., 1986. Earthquake prediction and electric signals. Nature 322, 120.
Vinet, P. et al., 1987. Compressibility of solids. J. Geophys. Res. 92, 9319–9325.
Warwick, J.W. et al., 1982. Radio emission associated with rock fracture: possible application to the great Chilean earthquake of May 22, 1960. J. Geophys. Res. 87, 2851–2859.
Wasa, Y., Wadatsumi, K., 2003. Functional strengthening and employment of Macroscopic Anomaly System by e-PISCO ASP. J. Jpn. Soc. Inf. Knowledge 13 (2), 41–47.
Xu, X.D. et al., 1991. Abnormal increase of satellite thermal infrared and ground surface temperature of impending earthquakes. Chin. Sci. Bull. 36 (4), 291–294.
Yasuoka, Y. et al., 2009. Preseismic changes in atmospheric radon concentration and crustal strain. Phys. Chem. Earth 34, 431–434.
Zakharenkova, I.E. et al., 2007. Features of the ionosphere behavior before the Kythira 2006 earthquake. Acta Geophys. 55 (4), 524–534.
Zhao, Y.L., Qian, F.Y., 1994. Geoelectric precursors to strong earthquakes in China. Tectonophysics 233, 99–113.
Zhao, Y., Qian, F., 2009. Impending HRT wave precursors to the Wenchuan Ms 8.0 earthquake and methods of earthquake impending prediction by using HRT wave. Sci. China, Ser. D: Earth Sci. 39 (1), 11–23.
Zlotnicki, J., Cornet, F.H., 1986. A numerical model of earthquake-induced piezomagnetic anomalies. J. Geophys. Res. B91, 709–718.